

Tropospheric BrO in the Arctic: satellite retrieval and ground-based data

H. Sihler et al.

Tropospheric BrO column densities in the Arctic from satellite: retrieval and comparison to ground-based measurements

H. Sihler^{1,2}, U. Platt², S. Beirle¹, T. Marbach³, S. Kühl¹, S. Dörner¹, J. Verschaeve⁴, U. Frieß², D. Pöhler², L. Vogel², R. Sander¹, and T. Wagner¹

¹Max Planck Institute for Chemistry, Hahn-Meitner-Weg 1, 55128 Mainz, Germany

²Institute of Environmental Physics, University of Heidelberg, Im Neuenheimer Feld 229, 69120 Heidelberg, Germany

³EUMETSAT, Eumetsat Allee 1, 64295 Darmstadt, Germany

⁴Norwegian Geotechnical Institute, Sognsveien 72, 0855 Oslo, Norway

Received: 28 March 2012 – Accepted: 20 April 2012 – Published: 3 May 2012

Correspondence to: H. Sihler (holger.sihler@mpic.de)

Published by Copernicus Publications on behalf of the European Geosciences Union.

Title Page

Abstract

Introduction

Conclusions

References

Tables

Figures

⏪

⏩

◀

▶

Back

Close

Full Screen / Esc

Printer-friendly Version

Interactive Discussion

Abstract

During polar spring, halogen radicals like bromine monoxide (BrO) play an important role in the chemistry of tropospheric ozone destruction. Satellite measurements of the BrO-distribution have become a particularly useful tool to investigate this probably natural phenomenon, but the separation of stratospheric and tropospheric partial columns of BrO is challenging. In this study, an algorithm was developed to retrieve tropospheric vertical column densities of BrO from data of high-resolution spectroscopic satellite instruments such as the second Global Ozone Monitoring Experiment (GOME-2). Unlike recently published approaches, the presented algorithm is capable of separating the fraction of BrO in the activated troposphere from the total BrO column solely based on remotely measured properties. The sensitivity of each satellite pixel to BrO in the boundary-layer is quantified using the measured UV-radiance and the column density of the oxygen collision complex O_4 . A comparison of the sensitivities with CALIPSO LIDAR observations demonstrates that clouds shielding near-surface trace-gas columns can be reliably detected even over ice and snow. Retrieved tropospheric BrO columns are then compared to ground-based BrO measurements from two Arctic field campaigns in the Amundsen Gulf and at Barrow in 2008 and 2009, respectively. Our algorithm was found to be capable of retrieving enhanced near-surface BrO during both campaigns in good agreement to ground-based data. Some differences between ground-based and satellite measurements observed at Barrow can be explained by both, elevated and shallow surface layers of BrO. The observations strongly suggest that surface release processes are the dominating source of BrO and that boundary-layer meteorology influences the vertical distribution.

1 Introduction

Barrie et al. (1988) discovered bromine activation as the phenomenon behind polar ozone depletion events (ODEs) in the Arctic troposphere. Since then, considerable

AMTD

5, 3199–3270, 2012

Tropospheric BrO in the Arctic: satellite retrieval and ground-based data

H. Sihler et al.

Title Page

Abstract

Introduction

Conclusions

References

Tables

Figures

⏪

⏩

◀

▶

Back

Close

Full Screen / Esc

Printer-friendly Version

Interactive Discussion



Tropospheric BrO in the Arctic: satellite retrieval and ground-based data

H. Sihler et al.

Title Page

Abstract

Introduction

Conclusions

References

Tables

Figures

⏪

⏩

◀

▶

Back

Close

Full Screen / Esc

Printer-friendly Version

Interactive Discussion



progress in understanding the phenomenon of ODEs has been made. However, even after two decades, key questions remain open: what are the sources of reactive halogens, what triggers their release, and what is the impact on the global tropospheric ozone budget? For a review of the current understanding of the halogen chemistry in the polar troposphere see also Simpson et al. (2007) and references therein.

Bromine monoxide (BrO) is a radical that catalytically destroys ozone. Its first observation from space was enabled by the Global Ozone Monitoring Experiment (GOME) instrument aboard the ERS-2 satellite (Wagner and Platt, 1998; Richter et al., 1998; Chance, 1998). Areas up to 2000 km across (covering several million km²) with elevated columns of BrO were detected to appear from one day to another implying local production of BrO. BrO is remotely probed from space by the technique of differential optical absorption spectroscopy (DOAS) which uses characteristic narrow absorption bands of molecules (Platt and Stutz, 2008).

Compared to ground-based measurement techniques like LP-DOAS (Tuckermann et al., 1997; Hausmann and Platt, 1994; Hönninger et al., 2004; Pöhler et al., 2010; Liao et al., 2011), MAX-DOAS (Hönninger and Platt, 2002; Hönninger et al., 2004; Wagner et al., 2007; Frieß et al., 2011), or CIMS (Liao et al., 2011), observations from space offer a much better spatial coverage (polar regions reach about full coverage once per day) while temporal resolution and information about the vertical distribution is comparatively sparse. Another advantage of satellite instruments is the relatively long time of operation of several years. Satellite data-sets are particularly suitable to answer open questions or test hypotheses on a more general basis (Wagner et al., 2001; Richter et al., 2002; Hollwedel et al., 2004; Kaleschke et al., 2004).

Before an existing data set on BrO column densities can be analyzed for tropospheric BrO activation, systematic errors need to be minimized. One of the largest uncertainties comes from the variability of the stratospheric BrO column (Wagner and Platt, 1998; Wagner, 1999; Theys et al., 2009; Salawitch et al., 2010; Choi et al., 2011) which needs to be assessed in order to study BrO in the troposphere from satellite observations. For extremely low tropopause heights, the stratospheric partial column

Tropospheric BrO in the Arctic: satellite retrieval and ground-based data

H. Sihler et al.

[Title Page](#)[Abstract](#)[Introduction](#)[Conclusions](#)[References](#)[Tables](#)[Figures](#)[⏪](#)[⏩](#)[◀](#)[▶](#)[Back](#)[Close](#)[Full Screen / Esc](#)[Printer-friendly Version](#)[Interactive Discussion](#)

may become comparable to that of a tropospheric event. When the tropopause lowers, the stratospheric air is adiabatically compressed and hence the stratospheric column of BrO increases additionally to an increase of the overall thickness of the stratosphere. Spatial structures mimicing tropospheric bromine events may thus appear in maps of the total BrO column. The challenge is to separate possible tropospheric events from stratospheric disturbances.

Several retrievals of tropospheric BrO columns use the output of stratospheric chemistry models for stratospheric BrO correction (Theys et al., 2009, 2011; Begoin et al., 2010; Salawitch et al., 2010; Toyota et al., 2011; Choi et al., 2011). These algorithms are either using simulated stratospheric columns of BrO directly or derive a parameterisation of the stratospheric BrO column based on model results first and then apply a climatology from which the stratospheric BrO column is calculated using measured O₃ and NO₂ column data. However, chemistry models are potentially biased because the chemical mechanisms may be incomplete, and necessary parameterisations may result in systematic errors. Model results also depend on the choice of initial values which are usually difficult to obtain.

The retrieval proposed in this work overcomes these drawbacks by retrieving the parameters to estimate the stratospheric BrO column using only the measurements themselves. In brief, our algorithm uses the simultaneously retrieved O₃ column density to account for dynamic effects and the retrieved NO₂ column density to account for chemical effects. The algorithm contains the following four steps (details are given in Sect. 2.2): first, the column measurements of BrO and O₃ are binned according to the respective NO₂ column, the solar zenith angle, and the line of sight angle. In a second step, the measurements without a significantly enhanced BrO/O₃ column ratio are considered to calculate the mean stratospheric BrO/O₃ column ratio within each bin. Then, the stratospheric BrO column for each pixel is calculated using the measured O₃ and NO₂ column densities and the solar zenith angle. Finally, the difference between measured total and calculated stratospheric column yields a residual BrO column. This approach is completely independent from models.

Tropospheric BrO in the Arctic: satellite retrieval and ground-based data

H. Sihler et al.

[Title Page](#)[Abstract](#)[Introduction](#)[Conclusions](#)[References](#)[Tables](#)[Figures](#)[⏪](#)[⏩](#)[◀](#)[▶](#)[Back](#)[Close](#)[Full Screen / Esc](#)[Printer-friendly Version](#)[Interactive Discussion](#)

In a second step, an algorithm assuring the sensitivity of the satellite measurement towards BrO located in the boundary-layer (BL) is developed and also included in the retrieval. Hence, it is possible to study surface processes involved in bromine activation on a per-pixel basis. Parameters affecting this sensitivity are the surface albedo as well as the thickness and height of overlying clouds. In polar regions, the detection of clouds from satellites is particularly difficult for instruments measuring in the UV and visible spectral range due to ambiguities between cloud particles and the ice- or snow-covered underlying surface. Various studies to measure optical properties of clouds over ice in polar regions from space (e.g. Vasilkov et al., 2010; O'Byrne et al., 2010) are based on data from a multitude of sensors and satellites. The ice-mode of FRESKO+ (Wang et al., 2008) derives the surface height of an Lambertian reflector with monthly averaged climatological albedo value using O₂ absorption measurements. In this work, we chose a slightly different approach: individual reflectances are combined with the corresponding differential absorption of the (O₂)₂ collision complex (denoted O₄ in this work) in order to assure the sensitivity above a given threshold. The scale height of O₄ is approx. 4 km (Greenblatt et al., 1990; Acarreta et al., 2004) thus providing a better sensitivity to near-surface concentrations compared to O₂.

This paper is organized as follows: in Sect. 2 we describe our new algorithm to retrieve tropospheric columns of BrO during periods of halogen activation in Arctic spring. Different parts of the algorithm are either compared to simulated data or measurements from other satellite instruments in Sect. 3. Retrieved tropospheric BrO columns are compared with ground-based measurements of BrO obtained during two field campaigns to the Arctic in 2008 and 2009 (Sect. 4). Conclusions are drawn in Sect. 5.

2 Spectral evaluation, column separation and sensitivity filter

The GOME-2 instrument (second Global Ozone Monitoring Experiment) is a high-resolution nadir scanning spectrometer aboard the MetOp-A satellite (e.g. Callies et al., 2000; Munro et al., 2006). MetOp-A, launched in 2006, is the first of a series of three

polar-orbiting satellites of identical design. The satellite is flying in a sun-synchronous orbit crossing the Equator at 09:30 LT. It is a platform for a set of instruments primarily designed for meteorological applications. Data from two of these instruments – the AVHRR (Advanced Very High Resolution Radiometer) and GOME-2 – are used in this study. The retrieval of tropospheric columns of BrO from GOME-2 is the main focus, while AVHRR data will later be applied to evaluate the sensitivity to near-surface trace-gas concentrations (Sect. 3.2).

GOME-2 has four main spectral channels in the UV/vis spectral range between 240 and 790 nm. The instrument is scanning in a whisk-broom scheme with a swath-width of 1920 km, which allows an almost global coverage each day. Polar regions, however, are sampled several times a day. The nominal ground pixel size is approx. $80 \times 40 \text{ km}^2$ with an integration time of 187.5 ms per spectrum.

Three fundamental steps are needed in order to retrieve a residual tropospheric vertical column density of BrO (VCD_{trop}) from GOME-2 spectra:

- i. Retrieval of total slant column densities (SCDs) of BrO, O_3 , NO_2 , and O_4 from Earth radiance spectra using the DOAS method (Sect. 2.1).
- ii. Separation into a stratospheric and residual tropospheric BrO SCD (Sect. 2.2). The main concept behind the algorithm is described in Sect. 2.2.1 followed by its implementation in Sect. 2.2.2.
- iii. Calculation of VCD_{trop} using a tropospheric air-mass factor (AMF) retrieved from O_4 -SCD and reflectance measurements (Sect. 2.3). The algorithm, which is also capable to filter measurements with a low sensitivity to near-surface concentrations of BrO, is described in Sect. 2.3.1, and its implementation in Sect. 2.3.2.

The results from the retrieval as well as its advantages and disadvantages are discussed in Sect. 2.4.

Tropospheric BrO in the Arctic: satellite retrieval and ground-based data

H. Sihler et al.

Title Page

Abstract

Introduction

Conclusions

References

Tables

Figures

⏪

⏩

◀

▶

Back

Close

Full Screen / Esc

Printer-friendly Version

Interactive Discussion



2.1 Evaluation of GOME-2 spectra

Differential optical absorption spectroscopy (DOAS) is a common technique to derive slant column densities of numerous trace-gases in the atmosphere (Platt and Stutz, 2008). In this work, DOAS is applied in three different wavelength ranges to derive SCDs of BrO, O₃, O₄ and NO₂ from calibrated GOME-2 spectra. Table 1 summarizes the parameters and molecular absorption cross-sections applied in the DOAS evaluation.

For the retrieval of BrO SCDs, several modifications compared to previously published retrievals are applied to the settings of the DOAS fit. The wavelength range between 336 and 360 nm combines the standard wavelength ranges used for GOME (Wagner and Platt, 1998; Aliwell et al., 2002) and SCIAMACHY (Afe et al., 2004; De Smedt et al., 2004) and encompasses four absorption bands of the BrO molecule. Furthermore, formaldehyde (HCHO) was excluded from the spectral evaluation in order to reduce the noise level of the BrO retrieval. This approach is appropriate when only polar regions are taken into account where HCHO abundances are generally low. In addition to molecular absorption cross-sections, two spectra are included in the evaluation procedure to account for the wavelength dependent Ring effect (Grainger and Ring, 1962) following the suggestions of Wagner et al. (2009a); both are calculated and normalized using the DOASIS software version 3.2 (Kraus, 2004). Furthermore, a reciprocal intensity spectrum is included in the fit in order to account for possible stray light within the instrument. A fourth-order polynomial is finally included to account for broad-band effects like surface reflection as well as Mie and Rayleigh scattering.

The fit result furnish us with total SCDs of BrO S . Total VCDs V of BrO can be approximated from S using

$$V = \frac{S}{A_{\text{geom}}} \quad (1)$$

Tropospheric BrO in the Arctic: satellite retrieval and ground-based data

H. Sihler et al.

Title Page

Abstract

Introduction

Conclusions

References

Tables

Figures



Back

Close

Full Screen / Esc

Printer-friendly Version

Interactive Discussion



by applying a geometric air-mass factor A_{geom} . While the AMF is defined as the ratio of SCD and VCD in general, A_{geom} displays an adequate approximation for stratospheric absorbers for $\text{SZA} < 80^\circ$. It is defined as

$$A_{\text{geom}} = \frac{1}{\cos \vartheta} + \frac{1}{\cos \psi}. \quad (2)$$

where ϑ denotes the SZA, and ψ denotes the line-of-sight (LOS) angle. As an example, total VCDs of BrO measured on 25 March 2009 over the Arctic are plotted in Fig. 1a.

Owing to the strong differential structure of ozone, the SCD of O_3 may also be derived from the same DOAS evaluation as BrO at much higher signal-to-noise ratio. The O_3 -SCD is calculated as the sum of the fit results of both O_3 references corresponding to different temperatures. This approach of a retrieval for O_3 potentially leads to SCDs with a systematic error which, however, cancels out later during the parameterisation of the stratospheric BrO-column (Sect. 2.2). O_3 VCDs computed from O_3 -SCDs and a geometric AMF are shown in Fig. 1b for 25 March 2009.

Using radiances in another wavelength interval, the SCD of the oxygen collision complex (O_4) is retrieved in the range between 355 and 390 nm using the setting compiled in Table 1. This spectral range includes two absorption bands of O_4 at 360 nm and 380 nm.

Finally, the SCD of NO_2 is retrieved from radiances measured in Band 4 of the GOME-2 instrument in the range between 431 nm and 453 nm. In contrast to the previous two settings, a single Ring spectrum (also calculated using the DOASIS software) was found to be sufficient due to a weaker Raman signal at longer wavelengths in connection with the rather narrow fit range.

Tropospheric BrO in the Arctic: satellite retrieval and ground-based data

H. Sihler et al.

Title Page

Abstract

Introduction

Conclusions

References

Tables

Figures

⏪

⏩

◀

▶

Back

Close

Full Screen / Esc

Printer-friendly Version

Interactive Discussion

2.2 Separation of tropospheric and stratospheric BrO slant-columns

This section describes how the measured total SCD of BrO is separated into background stratospheric and residual tropospheric column density S_{strat} and S_{trop} , respectively.

$$S = S_{\text{strat}} + S_{\text{trop}} \quad (3)$$

Furthermore, the standard deviation of the measurement σ_0 of BrO is estimated. This allows to evaluate the significance of a possible tropospheric signal. For the sake of clarity, SCDs S and VCDs V without subscripted chemical formula denote BrO column densities throughout the paper.

2.2.1 Concept of the BrO column separation

The main task of the BrO column separation is to compute the SCD of BrO contained in the stratosphere, S_{strat} . O_3 is chosen as a tracer for the stratospheric partial column. The ratio z_0 of the stratospheric BrO SCD to the O_3 SCD, $S_{\text{strat},\text{O}_3}$ is defined as

$$z_0 = \frac{S_{\text{strat}}}{S_{\text{strat},\text{O}_3}} \quad (4)$$

Knowing z_0 and $S_{\text{strat},\text{O}_3}$ would allow us to compute the SCD of BrO directly:

$$S_{\text{strat}} = S_{\text{strat},\text{O}_3} \cdot z_0 \quad (5)$$

However, measurement data obtained by GOME-2 furnishes us only with a set of values of the ratio z between the total BrO-SCD S and of the total O_3 -SCD S_{O_3} in the stratosphere and troposphere combined:

$$z = \frac{S}{S_{\text{O}_3}} \quad (6)$$

Tropospheric BrO in the Arctic: satellite retrieval and ground-based data

H. Sihler et al.

Title Page

Abstract

Introduction

Conclusions

References

Tables

Figures

◀

▶

◀

▶

Back

Close

Full Screen / Esc

Printer-friendly Version

Interactive Discussion



As a result, the ratio z_0 of BrO SCD to O₃ SCD in Eq. (4) decreases with increasing concentration of NO₂ also depending on the SZA ϑ determining the actinic flux. The concentration of NO₂ is not accessible from nadir measurements alone and therefore the NO₂ vertical column density V_N is used in the column separation process instead.

Furthermore, our algorithm also accounts for a slight dependence of z_0 on the line-of-sight (LOS) angle ψ . The stratospheric BrO SCD S_{strat} is therefore mainly a function of ϑ , V_N , and ψ :

$$S_{\text{strat}}(\vartheta, V_N, \psi) = S_{\text{strat}, \text{O}_3} \cdot \bar{z}_0(\vartheta, V_N, \psi). \quad (10)$$

Although the stratospheric AMFs of BrO and O₃ are similar, Eq. (10) can, in addition, also compensate differences of both AMFs since \bar{z}_0 depends also on ϑ and ψ . Unfortunately, however, the assumptions made so far are not applicable to the chemistry inside the polar vortex and during ozone-hole conditions. Extremely cold temperatures alter the chemistry of the stratosphere rendering reaction Eq. (9) insufficient to describe the chemistry affecting BrO. Moreover, there can be massive chemical loss of stratospheric O₃ thus $S_{\text{strat}, \text{O}_3}$ can no longer be used to account for dynamical effects. Therefore, our algorithm in its present form is inapplicable for an estimation of the stratospheric BrO within the polar vortex occurring in springtime Antarctica in general and in some areas of the Northern Hemisphere during winters with low stratospheric temperatures as depicted in Fig. 2.

Finally, in order to compute S_{strat} as a function of ϑ , V_N , and ψ , we need to compute $\bar{z}_0(\vartheta, V_N, \psi)$ from

$$z(\vartheta, V_N, \psi) = \bar{z}_0(\vartheta, V_N, \psi) + \zeta_{\sigma(\vartheta, V_N, \psi)} + z'(\vartheta, V_N, \psi). \quad (11)$$

The precise procedure how this is done is explained in the following subsection.

2.2.2 Implementation of the column separation algorithm

This section describes the implementation of the algorithm to calculate the tropospheric SCD of BrO. The algorithm is divided into four steps: (i) normalization of the BrO SCDs,

Tropospheric BrO in the Arctic: satellite retrieval and ground-based data

H. Sihler et al.

Title Page

Abstract

Introduction

Conclusions

References

Tables

Figures

◀

▶

◀

▶

Back

Close

Full Screen / Esc

Printer-friendly Version

Interactive Discussion

(ii) selection of reference measurements for one day and partitioning of reference measurements in the (ϑ, V_N) -plane for five different ψ -ranges, (iii) calculation of a mean background stratospheric BrO/O₃-SCD ratio \bar{z}_0 in each partition after filtering significantly enhanced ratios, and (iv) mapping of $\bar{z}_0(\vartheta, V_N, \psi)$ on all observations and calculation of the stratospheric BrO SCD according to Eq. (10).

The statistical analysis to retrieve \bar{z}_0 requires a sufficiently large base population of measurements T_0 . The analysis is performed separately for each day D . In order to increase the size of T_0 all measurements within a 7-day period $P = [D - 3, D + 3]$ are considered. This approach improves the statistical significance and reduces noise. It is similar to a running average filter and can be justified since the stratospheric chemistry usually only changes slightly within one week.

i. Measured BrO SCDs are normalized to a VCD of $V_{\text{norm}} = 3.5 \times 10^{13} \text{ molec cm}^{-2}$ within a reference sector over the Pacific Ocean as suggested by Richter et al. (2002). This normalisation is performed for each pixel-number of one scan separately (GOME-2: 32 pixels per scan, pixel-numbers correspond to discrete LOS angles). The boundaries of the reference sector are $\pm 10^\circ$ latitude and 150° E to 100° W longitude. Pixels with a footprint significantly different from the nominal $\approx 80 \times 40 \text{ km}^2$ (narrow-mode and backscan pixels) are excluded from counting as reference measurements. The normalized SCDs S are calculated by subtracting the median difference between SCDs in the reference sector and the normalized SCD $S_{\text{norm}} = V_{\text{norm}} \cdot A_{\text{geom}}$ from the measured SCDs.

ii. A subset $T \subset T_0$ of measurements is selected to avoid interferences with anthropogenic NO₂ emissions and to increase the accuracy of the stratospheric information in the nadir observations. T , from which the stratospheric correction is computed, contains only those observations with an SZA smaller than 80° , latitudes above 30° N , a fit-error for BrO smaller than $5 \times 10^{13} \text{ molec cm}^{-2}$, an O₄-SCD larger than $6.5 \times 10^{42} \text{ molec}^2 \text{ cm}^{-5}$, a non-negative NO₂ VCD smaller than $8 \times 10^{15} \text{ molec cm}^{-2}$ below 60° N . Narrow-mode and backscan pixels are excluded

Tropospheric BrO in the Arctic: satellite retrieval and ground-based data

H. Sihler et al.

Title Page

Abstract

Introduction

Conclusions

References

Tables

Figures

◀

▶

◀

▶

Back

Close

Full Screen / Esc

Printer-friendly Version

Interactive Discussion



from T as well as potential measurements within the polar vortex, as for example depicted in Fig. 2f. Areas inside the polar vortex are identified using information about the potential vorticity derived from meteorological model data (ECMWF operational analysis, regular $1^\circ \times 1^\circ$ grid with 91 hybrid pressure levels, 6 h time resolution). Columns exceeding a potential vorticity of 35 PVU at the 475 K isentrope surface or 75 PVU at 550 K are discarded from the further analysis. Furthermore, T does not contain any measurements with a ground elevation above 1000 m and no measurements over land masses at latitudes below 73° N. The latter selection rule accounts for areas with a strong anthropogenic NO_2 signal like Prudhoe Bay or Norilsk which would interfere with the algorithm. After applying these filters, the final subset T contains $N_\alpha \approx 10^5$ reference observations for each day from which the stratospheric BrO column is estimated. The geographical area encompassing T is illustrated in Fig. 3.

- iii. A mean stratospheric BrO/ O_3 ratio $\bar{z}_0(\vartheta, V_N, \psi)$ is calculated from T . Obtaining an estimate of \bar{z}_0 , Eq. (11), by measured values of $z_\alpha \in T$ with coordinates $(\vartheta_\alpha, V_{N_\alpha}, \psi_\alpha)$, $\alpha = 1, \dots, N_\alpha$, containing an arbitrary error with a Gaussian and a positive unknown contribution, requires a technique of approximating a function on an unstructured set of points where the data to be approximated contains uncertainties. Traditionally, least-squares approximations (Quarteroni et al., 2002) are used to approximate scattered data. More elaborate methods use radial basis functions or Kriging (Press et al., 2007) in order to treat scattered data. Common to these methods is that some knowledge about the distribution, such as the variance, is necessary in order to compute an approximant. In addition, they are relatively costly, given that the number of measured values N_α is large ($\approx 10^5$), making it necessary to have an efficient method to process a large number of these data sets.

For the method proposed in the present discussion, we take advantage of the fact that the function $\bar{z}_0(\vartheta, V_N, \psi)$ depends only slowly on ϑ , V_N , and ψ . In addition, we use trilinear interpolation in order to avoid spurious oscillations which can occur

Tropospheric BrO in the Arctic: satellite retrieval and ground-based data

H. Sihler et al.

Title Page

Abstract

Introduction

Conclusions

References

Tables

Figures

◀

▶

◀

▶

Back

Close

Full Screen / Esc

Printer-friendly Version

Interactive Discussion



when using polynomials of higher degree. Since \bar{z}_0 depends only slowly on ϑ , V_N , and ψ , we can regroup the points at which z is given in subsets for which \bar{z}_0 is almost constant. For a domain $\Omega = [\vartheta_a, \vartheta_b] \times [V_{N_a}, V_{N_b}] \times [\psi_a, \psi_b]$, this boils down to finding a partition Ω_β , $\beta = 1, \dots, N_\beta$ of Ω , such that Ω_β contains enough points to allow for statistics on z_α for which $(\vartheta_\alpha, V_{N_\alpha}, \psi_\alpha) \in \Omega_\beta$. On the other hand, Ω_β should be small enough, such that \bar{z}_0 does not vary too much with respect to ϑ , V_N , and ψ in Ω_β . It is clear that such a partition, as shown in Fig. 4, is not unique and that the shape of the subsets Ω_β might influence the accuracy of the present method. In Appendix A, we present in more detail how Ω is partitioned in quadrilaterals, allowing a trilinear reconstruction of \bar{z}_0 .

For each partition Ω_β , a filter algorithm is applied as presented in the following. The filter algorithm is based on the assumption that an ensemble of z , Eq. (11), is normally distributed around \bar{z}_0 . Significant outliers, if any, are mostly due to enhancements of the tropospheric BrO column and to a lesser degree, due to a partially depleted O_3 column. Both effects lead to an increase of a particular z by z' in Eq. (11), which in turn leads to an increasing asymmetry of the otherwise symmetric normal distributed z (Fig. 5). The asymmetry a_β of the distribution of $z = z(\Omega_\beta)$ in partition Ω_β is defined as

$$a_\beta(z) = \frac{\bar{z} - \tilde{z}}{\sigma}, \quad (12)$$

where \bar{z} denotes the mean, \tilde{z} the median, σ the standard deviation of z . If a_β is larger than a threshold, i.e. the distribution is skewed towards higher BrO/ O_3 SCD ratios, a subset of z accounting for the stratosphere needs to be calculated before \bar{z} and σ can be used as estimators for \bar{z}_0 and the standard deviation σ_0 of z_0 , respectively.

A filter algorithm is designed to find a subset of z with a symmetric distribution identified as the *stratospheric mode* (Fig. 5). The asymmetry of the distribution of z is iteratively minimized by cropping values with an offset $\Delta z = |z - \bar{z}|$ larger

Tropospheric BrO in the Arctic: satellite retrieval and ground-based data

H. Sihler et al.

Title Page

Abstract

Introduction

Conclusions

References

Tables

Figures

◀

▶

◀

▶

Back

Close

Full Screen / Esc

Printer-friendly Version

Interactive Discussion

than a given threshold δz . In step k of the iteration, the asymmetry a_k of the distribution of

$$z_k = \{z \mid -\delta z_k < z - \bar{z}_{k-1} < \delta z_k\} \quad (13)$$

is calculated with \bar{z}_{k-1} denoting the mean of the distribution in the previous step. Starting with $\delta z_0 = \max(z) - \bar{z}$, the threshold δz_k is iteratively decreased until $a_k \leq 0.001$ or a maximum of $k = 20$ steps is reached (see green bars in Fig. 5). The minimal asymmetry calculated from this algorithm is limited by numerical accuracy and the termination condition of 0.001 was found to provide still a reasonable small residual asymmetry of the output. The result is a filtered mean $\bar{z}_\beta = \bar{z}_k$. The standard deviation σ_β , however, is not calculated based on the cropped distribution of z_k . This approach would lead to an underestimation of the true standard deviation because the cropped distribution (green bars in Fig. 5) has a larger kurtosis than the normal distribution. Therefore, it is computed only using measurements with $z_m < \bar{z}_\beta$

$$\sigma_\beta = \sqrt{\frac{1}{n-1} \sum_m (z_m - \bar{z}_k)^2} \quad (14)$$

because this selection is assumed not to include any measurements with a significant tropospheric signal.

- iv. The above computed values \bar{z}_β and σ_β are mapped to the center of gravity of the points $(\vartheta_\alpha, V_{N_\alpha}, \psi_\alpha)$ in Ω_β and used for trilinear interpolation, which furnishes us two functions $\bar{z}_0(\vartheta, V_N, \psi)$ and $\sigma_0(\vartheta, V_N, \psi)$. Now the SCD of BrO in the stratosphere S_{strat} and its standard deviation, σ_{strat} can be computed by:

$$S_{\text{strat}} = S_{\text{strat}, \text{O}_3} \cdot \bar{z}_0(\vartheta, V_N, \psi), \quad (15)$$

$$\sigma_{\text{strat}} = S_{\text{strat}, \text{O}_3} \cdot \sigma_0(\vartheta, V_N, \psi). \quad (16)$$

Tropospheric BrO in the Arctic: satellite retrieval and ground-based data

H. Sihler et al.

Title Page

Abstract

Introduction

Conclusions

References

Tables

Figures

⏪

⏩

◀

▶

Back

Close

Full Screen / Esc

Printer-friendly Version

Interactive Discussion



As an example, Figs. 1e and 2e illustrate the resulting tropospheric BrO VCD for 25 March 2009 and 1 April 2008, respectively. It is interesting to note that, as depicted in Fig. 6a, the retrieved BrO/O₃ SCD ratio increases markedly from $< 4.8 \times 10^{-6}$ to $> 5.5 \times 10^{-6}$ for NO₂ VCDs below 2×10^{15} molec cm⁻² at high solar zenith angles. This observation confirms the predictions of the simple model for stratospheric chemistry mentioned above. Normally, NO₂ is a sink for stratospheric BrO leading to an anticorrelation between BrO and NO₂. Therefore, the abundance of BrO is enhanced with respect to O₃ at low NO₂ concentrations.

The detailed steps of the partitioning algorithm are presented in Appendix A.

2.3 Sensitivity filter and air-mass factor

In order to finally retrieve the desired residual tropospheric VCD of BrO from the tropospheric SCD using

$$V_{\text{trop}} = \frac{S_{\text{trop}}}{A_{\text{trop}}} \quad (17)$$

we need to calculate the tropospheric air-mass factor A_{trop} . This section describes how A_{trop} can be retrieved from radiance measurements and O₄ SCDs and that each measurement can be classified into *sensitive* to the boundary-layer (BL) and *possibly obscured*. The concentration of O₄ is proportional to the square of the O₂ concentration and therefore its scale height is approximately 4 km. Hence, its absorption is a good indicator for the photons having penetrated the lower part of the atmosphere (e.g. Wagner and Platt, 1998).

2.3.1 Concept of the sensitivity filter

Ground-based measurements showed that most of the enhanced tropospheric BrO column is located within the BL and often close to the surface (e.g. Hönninger et al., 2004; Wagner et al., 2007; Pöhler et al., 2010; Prados-Roman et al., 2010; Frieß et al., 2011). We therefore assume, as an approximation, that the residual tropospheric column of BrO is entirely located between 0 and 500 m above the ground with a constant concentration (box profile). It is noted, that the exact value of the BrO mixed layer-height may differ in reality, but radiative transfer simulations showed its choice is not critical for the presented considerations. Therefore, instead of a real AMF_{trop} , the AMF for the lowest 500 m (AMF_{500} , denoted A_{500}) is retrieved and used in this work.

For nadir satellite observations, the sensitivity to the ground represented by AMF_{500} mostly depends on the surface albedo and whether clouds with a large cloud optical density (COD) are present. Under clear-sky conditions, the absorption signal from trace-gases located close to the ground is reduced over a dark surfaces due to little reflection by the ground compared to Rayleigh and Mie scattering in the atmosphere. But over bright surfaces, a substantial fraction of the observed photons penetrates near-surface layers. To a large extent, this is still true even for cloudy scenes. Thick clouds, however, effectively shield the absorption signal from these layers.

The distinction between sea-ice, snow, thick aerosol layers, water clouds, and ice clouds by satellite remote sensing is not unambiguously possible (Vasilkov et al., 2010) and therefore surface albedo and COD can not be readily derived from our measurements directly.

Instead, we chose an approach relying on proxies to parametrize AMF_{500} . The two proxies used in the proposed algorithm are the reflectance R and the O_4 AMF . R is calculated

$$R = \frac{L}{E} \quad (18)$$

Tropospheric BrO in the Arctic: satellite retrieval and ground-based data

H. Sihler et al.

Title Page

Abstract

Introduction

Conclusions

References

Tables

Figures

⏪

⏩

◀

▶

Back

Close

Full Screen / Esc

Printer-friendly Version

Interactive Discussion



where L and E are the Earth radiance and solar irradiance measured by GOME-2 at 372 nm, respectively. The wavelength of 372 nm for R was chosen in order to minimize interferences with trace-gases like O_4 absorbing in the same range. The O_4 AMF, A_0 , is calculated from the measured O_4 SCD S_{O_4} using the O_4 VCD integrated from sea level to the top of the atmosphere $V_{O_4} = 1.33 \times 10^{43} \text{ molec}^2 \text{ cm}^{-5}$

$$A_0 = \frac{S_{O_4}}{V_{O_4}} \cdot 0.8 \quad (19)$$

also applying an empirical correction factor of 0.8 which has already been suggested by Wagner et al. (2009b) and Cl  mer et al. (2010) and was confirmed by sensitivity studies conducted for this work. Figure 7b depicts A_0 measured on 25 March 2009.

Results from a computational radiative transfer model are used to study the interrelation between modelled values for R , A_0 and A_{500} . For this purpose, triples of (R, A_0, A_{500}) were modelled for a comprehensive set of surface albedos and aerosol/cloud scenarios. The main objective in the next step is to identify the range (or area in the (R, A_0) -plane) where an AMF_{500} exceeds a certain sensitivity threshold AMF_{500}^{\min} . The range limits are geometrically approximated, parameterised, and saved in look-up-tables (LUTs) for discrete viewing geometries. When finally analysing the measurements, the LUT parameters are interpolated depending on the viewing geometry. Whether a measurement fulfils the AMF_{500}^{\min} -criterion or not is then decided based on the measured R and A_0 .

Finally, the AMF for the boundary layer A_{500}^{meas} is derived from the same modelled values depending on R and A_0 . The parameters a_0 , a_x and a_y of the surface

$$A_{500}^{\text{meas}}(R, A_0) = a_0 + a_x \cdot R + a_y \cdot A_0 \quad (20)$$

are derived from a least-squares fit of a selection of modelled (R, A_0, A_{500}) -triples with $AMF_{500} > AMF_{500}^{\min}$. In analogy to the surface sensitivity algorithm, a_0 , a_x and a_y are also stored in LUTs.

Tropospheric BrO in the Arctic: satellite retrieval and ground-based data

H. Sihler et al.

Title Page

Abstract

Introduction

Conclusions

References

Tables

Figures

⏪

⏩

◀

▶

Back

Close

Full Screen / Esc

Printer-friendly Version

Interactive Discussion



2.3.2 Implementation of the sensitivity filter and AMF calculation

This section describes the implementation of the surface sensitivity filter algorithm. For each set of viewing geometries, the algorithm consists of five steps: (i) modelling of (R, A_0, A_{500}) -triplets for a fixed set of aerosol scenarios and surface albedos, (ii) interpolation of additional (R, A_0, A_{500}) -triplets accounting for partial cloud cover and different surface scenarios, (iii) parameterisation of the range of the (R, A_0) -plane where AMF_{500} exceeds a given threshold AMF_{500}^{\min} , (iv) derivation the a -parameters in Eq. (20), (v) allocation of derived parameters in look-up-tables. The LUTs are finally needed to interpolate the stored parameters for each GOME-2 pixel depending on its viewing geometry. The interpolated parameters are needed to decide whether a pixel is sensitive to the boundary layer and to calculate AMF_{500} using Eq. (20).

There are four parameters defining the satellite viewing geometry: the SZA ϑ , the solar relative azimuth angle (SRAA), the LOS angle ψ and the ground elevation. These parameters span the four dimensional LUTs whose discretisation nodes are summarized in Table 2. Each LUT has a total of 6720 entries corresponding to 6720 different viewing geometries.

- i. R, A_0 and AMF_{500} are modelled for different surface albedos and aerosol scenarios using the McArtim software package (Deutschmann et al., 2011). For each LUT entry, R, A_0 , and A_{500} are calculated for the albedos 0.03, 0.09, 0.24, 0.39, 0.54, 0.66, 0.78, 0.90, 0.96 for a pure Rayleigh atmosphere (clear-sky) and the aerosol/cloud scenarios summarized in Table 3. For the calculation of AMF_{500} , a tropospheric box profile between 0 and 500 m is assumed.
- ii. Further (R, A_0, A_{500}) -triplets are interpolated from the Monte Carlo model results for two reasons: firstly, interpolation increases the number of values populating the (R, A_0) -plane and hence increasing the accuracy of the subsequent parameterisation, and, secondly, through interpolation it may be accounted for real gradients of surface albedo and partial cloud cover. Large albedo gradients are typical for

Title Page

Abstract

Introduction

Conclusions

References

Tables

Figures

◀

▶

◀

▶

Back

Close

Full Screen / Esc

Printer-friendly Version

Interactive Discussion



Tropospheric BrO in the Arctic: satellite retrieval and ground-based data

H. Sihler et al.

Title Page

Abstract

Introduction

Conclusions

References

Tables

Figures

⏪

⏩

◀

▶

Back

Close

Full Screen / Esc

Printer-friendly Version

Interactive Discussion



ice-edges over oceans or areas of fresh-fallen snow over land. Therefore, the surface albedo is parameterised by two properties: the albedo at a wavelength of 372 nm and the high albedo fraction of the surface η_s .

η_s is the geometric fraction of the ground pixel assumed to have a very high albedo $R_{\text{high}} = 0.96$. The reflectance R defined by Eq. (18) then depends on η_s and the modelled reflectances R_{high} and R_{low} over surfaces with an albedo of 0.96 and below 0.96, respectively.

$$R(\eta_s) = (1 - \eta_s)R_{\text{low}} + \eta_s R_{\text{high}} \quad (21)$$

The number of photons crossing the boundary between both parts is assumed to be negligible (independent pixel approximation). Accordingly, the modelled AMF depends on η_s following

$$A(\eta_s) = \frac{(1 - \eta_s)R_{\text{low}}A_{\text{low}} + \eta_s R_{\text{high}}A_{\text{high}}}{(1 - \eta_s)R_{\text{low}} + \eta_s R_{\text{high}}} \quad (22)$$

where the modelled A_{low} and A_{high} are weighted by the modelled radiances (Martin et al., 2002).

Furthermore, scattering media in the atmosphere, i.e. clouds and/or aerosol layers, are modelled as a single layer with a geometric thickness of 1 km containing particles with a single scattering albedo of 1.00 and a Henyey-Greenstein asymmetry parameter of $g = 0.85$ (King, 1987). The parametrization of scattering media in our model atmosphere has three dimensions: the cloud fraction η_c , the cloud height (CH) and the cloud optical density (COD). η_c is defined as the fraction of a scenery which is covered by clouds. In analogy to the definition of η_s , photons are assumed to travel either through cloud-free (cf) or cloud-covered (cc) sceneries. The radiances and AMFs depending on the cloud-fraction may then be interpolated using

$$R(\eta_c) = (1 - \eta_c)R_{\text{cf}} + \eta_c R_{\text{cc}} \quad (23)$$

and

$$A(\eta_c) = \frac{(1 - \eta_c)R_{cf}A_{cf} + \eta_c R_{cc}A_{cc}}{(1 - \eta_c)R_{cf} + \eta_c R_{cc}} \quad (24)$$

respectively.

Summing up the interpolation steps for the radiance and both AMFs for fractional η_s and COD: (1) η_c is varied from 0.2 to 0.8 for every constant albedo using Eqs. (23) and (24), respectively. (2) For the clear-sky case, η_s ranges from 0.05 to 0.95 with steps of 0.05 using Eqs. (21) and (22), respectively. (3) With clouds, η_s and η_c were varied from 0 to 1 and from 0.2 to 1, respectively, both with steps of 0.2. This scheme results in 938 modelled and interpolated (R , A_0 , A_{500})-triplets. As an example, all triplets are shown in Fig. 8a for a nadir looking geometry and $SZA = 60^\circ$. R is plotted along the abscissa-axis and A_0 is plotted along the ordinate-axis. AMF_{500} values are color-coded. The comparison between modelled and measured (R, A_0)-pairs in Fig. 8b shows that the range of modelled values (for a specific viewing geometry) includes almost all corresponding measurements. Obviously, the numerical radiative transfer model McArtim is capable to reproduce the range of real measurements for the considered cloud scenarios.

- iii. The limits of range P in the (R , A_0)-plane containing AMF_{500} -values smaller than AMF_{500}^{\min} is parameterised. P is the inverse of the range where an AMF_{500} exceeding AMF_{500}^{\min} can be assured. The limits of P are geometrically approximated in order to obtain a suitable parameterisation. Therefore, a convex hull H containing all AMF_{500} smaller than AMF_{500}^{\min} is constructed.

As depicted by the shaded area in Fig. 8a, the characteristic shape of H enables us to approximate its upper edge with a parabola g

$$g(R) = g_0 + g_1 R + g_2 R^2. \quad (25)$$

Tropospheric BrO in the Arctic: satellite retrieval and ground-based data

H. Sihler et al.

Title Page

Abstract

Introduction

Conclusions

References

Tables

Figures

◀

▶

◀

▶

Back

Close

Full Screen / Esc

Printer-friendly Version

Interactive Discussion

Before g is approximated to the upper edge of H , we introduce an intensity threshold h . Using the reflectances of the upper right corner A and left corner B of H , R_A and R_B , respectively, h is given by the mean

$$h = (R_A + R_B)/2. \quad (26)$$

Finalizing the parameterisation of the edge, g is derived from a least-squares fit using the points of the upper edge of H with $R \geq h$.

- iv. A least-squares surface fit of all triples in the upper right section (greater than g , and h) is performed using the model function in Eq. (20).
- v. For a given AMF_{500}^{\min} , h , g_0 , g_1 , g_2 and the surface fit parameters a_0 , a_x and a_y are stored in seven separate LUTs, which are then used to interpolate the thresholds and $\text{AMF}_{500}^{\text{meas}}$ for any observation geometry for any measured R and A_0 .

Finally, an observation is flagged as *sensitive* if A_0 and R are larger than g and h , respectively, or otherwise as *possibly obscured*. If the measurement is sensitive, AMF_{500} is derived using interpolated values for a_0 , a_x and a_y .

2.4 Results and discussion of the retrieval algorithm

Tropospheric VCDs of BrO resulting from the column separation algorithm are displayed for 25 March 2009 in Fig. 1e and for 1 April 2007 in Fig. 2e. Both figures illustrate the capability of the algorithm to separate the residual tropospheric column from the measured total column and to reduce the correlation to the tropopause height on a large scale. Fine-structured areas of elevated BrO remain in the retrieved tropospheric columns. For 1 April 2007, the pixels in the east sector fall into areas where the O_3 VCDs are reduced due to ozone hole conditions. These are removed from the retrieval.

Figure 7 shows the tropospheric BrO columns for different choices of the AMF_{500}^{\min} threshold. The algorithm successfully removes measurements over areas outside the

Tropospheric BrO in the Arctic: satellite retrieval and ground-based data

H. Sihler et al.

Title Page

Abstract

Introduction

Conclusions

References

Tables

Figures

◀

▶

◀

▶

Back

Close

Full Screen / Esc

Printer-friendly Version

Interactive Discussion



Arctic with a relatively low surface albedo. The comparison between Figs. 7c through 7f shows that the maps depend only slightly on the choice of AMF_{500}^{\min} .

It is important to note, that the presented algorithm – compared to previously published algorithms – depends neither on results from stratospheric chemistry models, gridded measurements from other satellite instruments nor surface albedo climatologies avoiding the disadvantages of using a potentially biased model description and possible short-term deviations from climatological values. Apart from the potential vorticity data provided by ECMWF to identify areas potentially disturbed by ozone hole chemistry, only data measured by the GOME-2 instrument is required.

Another distinct advantage of the column separation algorithm is, that measurement errors are derived based on observations and not based on the mathematical fit error of the SCD retrieval. As pointed out by Stutz and Platt (1996), the fit error may underestimate the true error in the presence of erroneous reference cross-section alignment and systematically structured residual spectra. However, these malicious influences are difficult to quantify. In this work, empirically derived measurement errors are derived in order to provide a realistic error estimation which also includes the error of the column separation. Hence, it is possible to decide whether a measured BrO column density significantly exceeds the stratospheric background in the SCD space. This can be particularly advantageous when calculating the correlation to independent data-sources by avoiding a systematic bias from potentially flawed assumptions of the vertical distribution and the state of the atmosphere which are necessary to solve the radiative transfer.

3 Validation

The last section described the methods of a new satellite retrieval for tropospheric BrO column densities. Several parameters of the implementation to separate the tropospheric from the total column and the sensitivity filter algorithm for the boundary layer were determined by numerical inspection. The algorithm proved to be stable and

Tropospheric BrO in the Arctic: satellite retrieval and ground-based data

H. Sihler et al.

Title Page

Abstract

Introduction

Conclusions

References

Tables

Figures

⏪

⏩

◀

▶

Back

Close

Full Screen / Esc

Printer-friendly Version

Interactive Discussion



Tropospheric BrO in the Arctic: satellite retrieval and ground-based data

H. Sihler et al.

Title Page

Abstract

Introduction

Conclusions

References

Tables

Figures

◀

▶

◀

▶

Back

Close

Full Screen / Esc

Printer-friendly Version

Interactive Discussion

varying the different parameters within reasonable limits resulted in minor variations of the result. Due to its complexity, however, it is especially important to validate the presented algorithm in order to unravel potential flaws.

A validation requires independent measurements. Unfortunately, for tropospheric BrO columns, there is no independent satellite data to compare with and therefore the different steps of the algorithm are validated separately using data from instruments other than GOME-2: (1) The decomposition algorithm of the total BrO column is tested on simulated measurements (Sect 3.1). (2) Results of the surface sensitivity filter are validated through a case study of imaging satellite data in the red spectral region (Sect. 3.2) and (3) compared to optical properties of clouds measured by the CALIOP instrument (Sect. 3.3). (4) The comparison of retrieved tropospheric VCDs to ground-based measurements of BrO, is described in Sect. 4. Additionally, (5) cross-validations to airborne DOAS measurements have already been published in Prados-Roman et al. (2010) and Heue et al. (2011).

3.1 Proof of concept of column separation algorithm using simulated measurements

In Sect. 2.2 we presented an algorithm to retrieve the ratio of stratospheric SCDs of BrO and O₃. The algorithm mainly consists of a two-dimensional partitioning of the measurements (Appendix A) and an asymmetry filter. Here, the capability of the algorithm to retrieve the true $\bar{z}_0(\vartheta, V_N)$ is benchmarked.

As a matter of fact, the true \bar{z}_0 is not known for the satellite nadir geometry. Therefore, the whole numerical algorithm is benchmarked using simulated measurements instead. The simulations are based on mathematical distributions without any a priori chemistry or radiative transfer. The retrieved \bar{z}_0 may then be compared to the known model function z_m used as an input for the measurement simulation.

Within the domain defined in Eq. (A2), we choose the surface

$$z_m : z = a\hat{x} \cos \hat{y} + b \quad (27)$$

Tropospheric BrO in the Arctic: satellite retrieval and ground-based data

H. Sihler et al.

Title Page

Abstract

Introduction

Conclusions

References

Tables

Figures

⏪

⏩

◀

▶

Back

Close

Full Screen / Esc

Printer-friendly Version

Interactive Discussion

with the normalised coordinates $\hat{x} = (\vartheta - 25^\circ)/55^\circ$ and $\hat{y} = V_N/(8 \times 10^{15} \text{ molec cm}^{-2})$ to model the stratospheric response of BrO/O₃-SCD ratio measurements (Fig. 9a). The parameters in Eq. (27) are $a = 5 \times 10^{-7}$ and $b = 4.9 \times 10^{-6}$, respectively. Then, 2×10^4 measurements of (ϑ, V_N, z) -triplets are simulated to sample z_m using several random-number generators.

The (ϑ, V_N) -plane is populated by two normal distributions as displayed in Fig. 9b. Then, for each (\hat{x}, \hat{y}) -pair, a normally distributed “tropospheric” value centred around 0 with a standard deviation $\sigma_{z,1} = 0.4 \times 10^{-7}$ is added to the respective value of z_m . Additionally, normally distributed values ($\sigma_{z,2} = 1.5 \times 10^{-6}$, offset $\Delta z_2 = 1.5 \times 10^{-6}$) are added to 15 % of the measurements to model events of enhanced BrO/O₃-fractions. As an example, the resulting distribution of z of measurements falling within the interval centred at $\vartheta = 70.9^\circ$ and $V_N = 2.2 \times 10^{15} \text{ molec cm}^{-2}$ is shown in Fig. 9d.

After the generation of measurements, the algorithm to derive BrO/O₃-fractions is applied as described in Sect. 2.2. The results are compiled in Fig. 9 with axes similar to Figs. 4, 5, and 6, respectively. The difference between z_m and the retrieved surface \bar{z}_0 and the relative error σ_0 are illustrated in Figs. 9e and 9f, respectively. Both plots show that the algorithm succeeds in reproducing the model function within the sampled area. Residual linear structures of the difference are artefacts caused by the bilinear interpolation between the nodes of retrieved surface. The relative error almost never ($< 1\%$) exceeds 2 % and the relative mean error is 0.5 %.

In conclusion, the presented algorithm is capable to reproduce a given model surface for the stratospheric BrO/O₃-SCD ratio within the sampled area. The described simulator was used to test different combinations of parameters for the algorithm (number of nodes, partitioning scheme, interpolation method, convergence thresholds). The final implementation of parameters was found to provide a reasonable trade-off between resolution and sampling error.

3.2 Comparison to AVHRR image data

As described in Sect. 2.3, the sensitivity of GOME-2 measurements to surface near trace-gas concentrations is difficult to quantify over sea-ice and snow covered land due to ambiguities in the optical properties of the surface (ice/snow) and clouds (water/ice).

5 However, by comparing the results of the presented sensitivity algorithm to AVHRR reflectance measurements it is possible to test the general response of the algorithm towards the shielding effect of (A) thin clouds over a dark lead, (B) thick clouds over ice, and (C) over only partially snow-covered land (Fig. 10).

10 The AVHRR/3 instrument is also borne by the MetOp-A satellite and measures reflectances at five spectral bands between the visible red and the thermal infra-red spectral range at a spatial resolution of 1.1 km. The black-and-white image in Fig. 10 shows AVHRR reflectance measurements at 630 nm (channel 1) of Northern Alaska and the Arctic Ocean from 4 April 2009 at 22:43:42 UTC. The scenery is dominated by large bright areas of sea-ice in the Bering Strait, the Arctic Ocean, as well as snow between the north coast of Alaska and the Brooks Range in the south. The color-coded outlines of individual satellite pixels represent pixels assured to be sensitive to the surface with $AMF_{500}^{\min} = 3$.

15 While the center of the satellite swath features the highest AMF_{500} (dark red pixels in the upper part), the algorithm manages to detect regions with a reduced sensitivity to the surface. Clearly, the sensitivity to the surface is reduced over dark surfaces like (A) the Barrow lead at the north-west coast of Alaska and (C) over the darker slopes of the Brooks Range to the bottom of the figure. A little bit more subtle (B) is the shielding effect of clouds in the east. The linear crack-like features in the sea-ice are almost completely blurred by clouds which can be identified by their shadows towards the north-west.

20

25

Tropospheric BrO in the Arctic: satellite retrieval and ground-based data

H. Sihler et al.

Title Page

Abstract

Introduction

Conclusions

References

Tables

Figures

⏪

⏩

◀

▶

Back

Close

Full Screen / Esc

Printer-friendly Version

Interactive Discussion



3.3 Comparison to CALIPSO cloud data

In order to validate the selectivity and response of the presented sensitivity filter (Sect. 2.3) towards clouds over bright surfaces, filter results are compared to measurements of the Cloud-Aerosol Lidar with Orthogonal Polarization (CALIOP) instrument. CALIOP is an active instrument measuring the time-resolved backscatter signal of a pulsed laser beam from which, among other parameters, the height and optical density of clouds may be derived independently from the surface albedo (NASA, 2006; Winker et al., 2007). CALIOP is the primary instrument carried by the Cloud-Aerosol Lidar and Infrared Pathfinder Satellite Observations (CALIPSO) satellite.

The specification of the satellites MetOp-A and CALIPSO and the measuring principle of the respective GOME-2 and CALIOP instruments differ fundamentally (see Table 4). The most dominant difference is the footprint of each instrument. CALIOP samples a single 70 m wide cross-section of the atmosphere while GOME-2 averages over 3200 km². CALIOP thus only probes 0.2 % of the atmospheric area within one GOME-2 pixel at most. A one-to-one comparison of GOME-2 and CALIOP measurements is therefore problematic but it is still possible to compare averages assuming the cloud properties CALIOP measures are to some extent representative for the whole GOME-2 pixel. Furthermore, CALIPSO flies on another orbit than MetOp-A. CALIPSO crosses the equator around 13:30 LT in ascending node while MetOp-A has an equator crossing time of 9:30 LT in descending node. In polar regions, however, the orbits of both satellites partly overlap. The time-difference between a CALIPSO and a MetOp-A overpass varies periodically and there are chances for almost simultaneous measurements.

In this study, four years of provisional CALIPSO Lidar Level 2 5 km cloud layer data are compared to the classification of GOME-2 pixels regarding the sensitivity to the surface (Sect. 2.3). The comparison focuses on the ability of the algorithm to detect clouds over bright surfaces possibly reducing the sensitivity to trace-gases at the surface. Therefore, only pixels featuring a high sea-ice concentration of 95 % are considered here. Sea-ice concentration maps derived from microwave-radar measurements were

Tropospheric BrO in the Arctic: satellite retrieval and ground-based data

H. Sihler et al.

Title Page

Abstract

Introduction

Conclusions

References

Tables

Figures



Back

Close

Full Screen / Esc

Printer-friendly Version

Interactive Discussion



Tropospheric BrO in the Arctic: satellite retrieval and ground-based data

H. Sihler et al.

Title Page

Abstract

Introduction

Conclusions

References

Tables

Figures

⏪

⏩

◀

▶

Back

Close

Full Screen / Esc

Printer-friendly Version

Interactive Discussion



provided by the Integrated Climate Data Center (ICDC), see Kaleschke et al. (2001) and Spreen et al. (2008) for a detailed description of the product. Additionally, only measurements in the Northern Hemisphere below 83° N latitude are compared. The time-difference between both measurements is limited to 30 min and every GOME-2 pixel taken into account must contain at least 70 km of the CALIPSO ground-track. Finally, 17 000 collocated measurements meet these selection criteria in the months February to June of the years 2007 to 2010.

Depending on AMF_{500}^{\min} , two properties of the CALIPSO data-set, the cloud optical thickness (COT) and layer top altitude (LTA) of the uppermost layer, are selected, averaged and classified following the sensitivity algorithm applied on the specific GOME-2 pixel they are collocated with. The resulting mean and median values are illustrated in Fig. 11. Within the limitations of a comparison of different data-sets, it can be concluded that the algorithm is capable to identify the shielding effect of clouds over sea-ice. Both the mean and the median cloud optical thickness of the sensitive pixels are always lower than of those classified as possibly obscured. A higher threshold AMF_{500}^{\min} increases the sensitivity of the filter towards filtering also thinner clouds, and an increase of AMF_{500}^{\min} leads to a decrease of the mean cloud optical thickness.

However, the mean layer top altitude was expected not to play such an important role because AMF_{500} is almost constant for clouds higher than 500 m. This dependence on AMF_{500}^{\min} may be due to the utilization of O_4 as a tracer whose SCD depends on the cloud top altitude also above 500 m. It is furthermore possible that this behaviour is an artefact caused by the limited sensitivity of the CALIOP instrument for large optical densities. The CALIPSO data may contain some cross-correlation between COT and LTA because higher clouds are potentially thicker than can be resolved by CALIOP.

3.4 Discussion of validation results

In this section, the column decomposition algorithm and the surface sensitivity filter algorithm were validated separately. Applied to simulated measurements, the different

Tropospheric BrO in the Arctic: satellite retrieval and ground-based data

H. Sihler et al.

Title Page

Abstract

Introduction

Conclusions

References

Tables

Figures

⏪

⏩

◀

▶

Back

Close

Full Screen / Esc

Printer-friendly Version

Interactive Discussion



components of the decomposition algorithm retrieved the correct values. This confirms the choice of parameters. Furthermore, results of the surface sensitivity filter algorithm were compared to two independent satellite data-sets. Firstly, a case-study using AVHRR image data showed that the filter algorithm manages to identify areas where the sensitivity to the surface is potentially decreased. Secondly, GOME-2 measurements over sea-ice were compared to CALIOP measurements providing information about the cloud cover.

From the comparison with CALIOP data it can be concluded that the filter algorithm is capable to detect clouds over sea-ice that are possibly reducing the sensitivity to near-surface absorbers. The filter threshold AMF_{500}^{\min} showed to have an influence on the median of both COT and LTA (Fig. 11).

Furthermore, the presented retrieval was compared to airborne MAX-DOAS measurements. Prados-Roman et al. (2010) presented measurements of BrO profiles obtained in the Arctic during the ASTAR campaign in spring 2007. Their results were compared to columns derived from the method by Theys et al. (2011) and the method presented here. All three data-sets were found consistent within the respective errors. In Heue et al. (2011), columns of SO_2 and BrO derived from GOME-2 measurements have been successfully compared to columns measured by the CARIBIC instrument analysing the plume of the Eyjafjallajökull volcano in May 2010. In the study by Heue et al. (2011), however, a different normalization procedure optimized for the detection of volcanic plumes on a regional scale was applied.

4 Comparison to ground-based measurements

In this section, tropospheric BrO VCDs from GOME-2 are compared to both LP-DOAS and MAX-DOAS measurements of BrO obtained during two Arctic field campaigns, respectively.

During March and April 2008, Pöhler et al. (2010) were measuring BrO in the tropospheric boundary layer directly over the sea-ice of the Amundsen Gulf from aboard the

Tropospheric BrO in the Arctic: satellite retrieval and ground-based data

H. Sihler et al.

Title Page

Abstract

Introduction

Conclusions

References

Tables

Figures

⏪

⏩

◀

▶

Back

Close

Full Screen / Esc

Printer-friendly Version

Interactive Discussion



Amundsen research ice-breaker. The data-set from the Amundsen includes long-path DOAS (LP-DOAS) and yet unpublished multi-axis DOAS (MAX-DOAS) measurements. The LP-DOAS was measuring concentrations of BrO averaged between 1 and 19 m height above the sea-ice. From MAX-DOAS measurements, BrO VCDs were calculated using the differential SCD between 10.6° and 90° divided by the differential AMF assuming clear-sky conditions and a surface albedo of 0.99 (Grenfell et al., 1994).

The other data-set was collected between March and April 2009 during the Ocean-Atmosphere Sea-Ice Snowpack (OASIS, <http://oasishome.net/>) field initiative at Barrow, Alaska. The LP-DOAS measurements were presented in Liao et al. (2011). Vertical profiles of BrO and aerosols were retrieved from MAX-DOAS data using optimal estimation as described by Frieß et al. (2011). Tropospheric BrO VCDs were determined by integrating the retrieved MAX-DOAS profiles.

Both, ground-based and satellite measurements offer their particular advantages and disadvantages to study the same phenomenon. Resolution and coverage differ between both approaches spatially and temporally. Ground-based instruments usually offer a higher spatial and temporal resolution whereas satellite measurements observe the same property over a vast area at moderate spatial and temporal resolution. In conclusion, a high correlation may only be expected if both techniques sample the same volume of air and spatial as well as temporal variabilities are small.

4.1 Collocating satellite data and ground-based measurements

In order to assure spatial and temporal coherence of ground-based and satellite measurements, coincident measurements have to be selected. Averages of collocated subsets are calculated for each overpass of the satellite. Note that a polar orbiting satellite may pass the same site several times a day during daylight depending on latitude, season, and type of swath. The swath of GOME-2 covers the studied sites up to three times a day at an SZA below 80°.

First of all, only those satellite measurements are selected which are sensitive to the ground (Sect. 2.3) and whose pixel footprint includes the location of the ground-based

measured up to 42 pmol mol^{-1} of BrO on 15 March when major enhancements were also observed by GOME-2 (see Supplement). The slope in Fig. 17b is approx. 500 m which represents an estimate for the BrO layer thickness.

The time series of both MAX-DOAS and LP-DOAS measurements at Barrow are shown in Figs. 15 and 16, respectively. More than a month of collocated measurements with GOME-2 from mid March to mid April 2009 are available. Compared to the measurements from aboard the Amundsen, the amplitudes of BrO enhancements (VCDs and mixing ratios) were generally smaller at Barrow. The correlations between GOME-2 and MAX-DOAS (Fig. 17c) as well as GOME-2 VCD and LP-DOAS mixing ratio (Fig. 17d) are weaker but statistically significant ($n = 77$, $r^2 = 0.1$, $p = 0.005$). The slope in Fig. 17c reveals that the BrO VCDs retrieved from MAX-DOAS measurements are approx. twice as high as the collocated GOME-2 measurements. However, the offset between both data sets is significantly smaller than for the Amundsen measurements.

It is important to note that the temporal variability of LP-DOAS mixing ratios at Barrow occasionally deviates from GOME-2 tropospheric VCDs (Fig. 16). There are several days where the LP-DOAS measured above 10 pmol mol^{-1} while the GOME-2 VCDs are close to zero (16, 23, 29 March, and 11 April). On 14 March, however, both GOME-2 and MAX-DOAS show significantly elevated BrO columns while the LP-DOAS measured comparatively moderate 7 pmol mol^{-1} . These differences are discussed in Sect. 4.3.

Finally, the dependence on the sensitivity threshold AMF_{500}^{\min} is studied. The correlation coefficient r^2 is calculated for all four ground-based data sets and collocated GOME-2 measurements for different AMF_{500}^{\min} between 0.5 and 4 (Fig. 18). Furthermore, the respective number of remaining collocated measurements are shown. As already mentioned, the correlation between satellite and ground-based measurements is larger for the Amundsen than for the Barrow data. The increase in r^2 with AMF_{500}^{\min} is consistent for both MAX-DOAS comparisons indicating that the proposed sensitivity filter in fact identifies measurements with ambiguous sensitivity (Fig. 18a and 18c).

Tropospheric BrO in the Arctic: satellite retrieval and ground-based data

H. Sihler et al.

Title Page

Abstract

Introduction

Conclusions

References

Tables

Figures

⏪

⏩

◀

▶

Back

Close

Full Screen / Esc

Printer-friendly Version

Interactive Discussion



Tropospheric BrO in the Arctic: satellite retrieval and ground-based data

H. Sihler et al.

Title Page	
Abstract	Introduction
Conclusions	References
Tables	Figures
⏪	⏩
◀	▶
Back	Close
Full Screen / Esc	
Printer-friendly Version	
Interactive Discussion	

For the LP-DOAS measurements, however, the trend for r^2 is less clear. For the Amundsen data, the correlation with LP-DOAS mixing ratios decreases significantly for $AMF_{500}^{\min} > 2$. At Barrow, r^2 increases only for rather high thresholds $AMF_{500}^{\min} \geq 3$ when more than half of the collocated measurements are filtered. For $AMF_{500}^{\min} = 3.2$ the correlation between LP-DOAS and GOME-2 is $r^2 = 0.19$ (see discussion below).

Gridded maps of daily satellite measurements corresponding to both time-series can be found in the Supplement to this paper.

4.3 Discussion of comparison with ground-based measurements

The comparisons between ground-based and satellite measurements of BrO show a good agreement, demonstrating the capability of the presented method to retrieve realistic tropospheric BrO column densities from GOME-2 measurements. The deviation from unity slopes for the correlation between GOME-2 VCDs and ground-based MAX-DOAS measurements for Amundsen and Barrow may be explained by a systematic difference of the sensitivity of both techniques with respect to the real distribution of BrO. The negative offset of GOME-2 VCDs compared to both MAX-DOAS time series possibly indicates that the presented algorithm underestimates the integrated tropospheric column. This systematic difference may be a result of the column separation algorithm (Sect. 2.2) for which it was assumed that the tropospheric column enhancement may reach zero. Hence, the negative offset indicates that there might be some residual BrO present almost everywhere in the Arctic during spring when also both presented LP-DOAS time series report significant BrO abundances every day (Pöhler et al., 2010; Liao et al., 2011). However, it is difficult to give a quantitative interpretation because both MAX-DOAS data sets were evaluated using different algorithms with different systematic errors. Furthermore, both MAX-DOAS and the GOME-2 retrieval apply different AMFs which may furthermore lead to systematic differences. E.g., the AMFs applied for the Amundsen measurements did not account for aerosol scattering which alters the sensitivity of the MAX-DOAS measurement with respect to GOME-2.



Tropospheric BrO in the Arctic: satellite retrieval and ground-based data

H. Sihler et al.

[Title Page](#)[Abstract](#)[Introduction](#)[Conclusions](#)[References](#)[Tables](#)[Figures](#)[⏪](#)[⏩](#)[◀](#)[▶](#)[Back](#)[Close](#)[Full Screen / Esc](#)[Printer-friendly Version](#)[Interactive Discussion](#)

The comparison of LP-DOAS measurements aboard the Amundsen in spring 2008 and GOME-2 VCDs clearly indicates that surface concentrations of BrO may provide significant contributions to the BrO column of more than 6×10^{13} molec cm^{-2} on 14 March. This corresponds to a surface BrO column extending to approx. 500 m altitude (Fig. 17b) in agreement with the height of the simultaneously measured O₃-depleted layer reported by Seabrook et al. (2011). The map of tropospheric BrO column densities (Fig. 14) shows a particularly large area affected by bromine activation. It is hence concluded, that this particular “BrO cloud” is located at the surface but not in elevated layers, at least not at the location of the Amundsen vessel.

At Barrow, however, the correlation between LP-DOAS and GOME-2 measurements was much weaker than seen on the Amundsen vessel. There are several potential explanations for this behaviour.

- i. The Barrow time series is much longer and the correlation comprises several strong events of elevated BrO levels. The height of the chemically perturbed boundary-layer varied strongly between these events (Frieß et al., 2011; Helmig et al., 2012). Therefore the assumption of a linear correlation may not be appropriate.
- ii. Located onshore, the local meteorology as well as surface processes related to bromine activation at Barrow may differ fundamentally from that over the sea ice. Furthermore, ground-based O₃ measurements at Barrow revealed large horizontal heterogeneities (Liao et al., 2011; Helmig et al., 2012) which may bias the LP-DOAS measurements with respect to the satellite.
- iii. The uncertainties of the sensitivity of the satellite measurement to the surface due to the nearby opening in the sea ice are large (cf. Sect. 3.2). In fact, increasing $\text{AMF}_{500}^{\text{min}}$ at Barrow resulted in an increased r^2 supporting this hypothesis. However, the comparison between MAX-DOAS and GOME-2 measurements at Barrow shows a good agreement despite the offset. Furthermore, the correlation of

surface concentrations as measured by LP-DOAS and retrieved from MAX-DOAS measurements is significant (Frieß et al., 2011, Fig. 3).

This indicates that the VCDs measured by GOME-2 are realistic and, hence, the variations of the BrO profile at Barrow were probably larger than during the Amundsen campaign where only one major event was captured by LP-DOAS. Occasionally enhanced near-surface BrO concentrations correspond to a shallower average mixing height of BrO as reproduced in Fig. 17d. In the following, two example days are selected in order to illustrate the vertical variability of the BrO profile.

As mentioned above, the LP-DOAS data in Fig. 16 show on several days considerably higher enhancements than GOME-2. This discrepancy can be explained by a very shallow layer of BrO (Fig. 19b). All shown MAX-DOAS profiles decrease to background values at altitude above 250 m.

Another interesting event was captured at Barrow on 14 March 2009. GOME-2 observed a significantly elevated BrO column while the LP-DOAS shows only moderate levels of bromine activation. However, the comparison with the integrated tropospheric VCD from MAX-DOAS again shows good agreement and the apparent discrepancy between LP-DOAS and GOME-2 therefore indicates the presence of an elevated layer of enhanced BrO concentrations as suggested by e.g. Hönninger and Platt (2002), Wagner et al. (2007), and Frieß et al. (2011). In this context, the term elevated denotes a layer of enhanced BrO at a few hundred metres which are still within the boundary-layer. On this day, O_3 levels were below 1 nmol mol^{-1} suggesting a limited production of BrO at the surface (Helmig et al., 2012). As sampled by an ozonesonde launched at Barrow (Fig. 19a), the O_3 mixing ratio increases with altitude allowing for a more efficient BrO production at these altitudes. Furthermore, the potential temperature gradient profile suggests a highly stratified boundary layer as well as a strong temperature inversion at the surface ($\sim 50 \text{ m}$) hampering O_3 mixing from aloft. This conclusion is supported by BrO profiles retrieved from MAX-DOAS measurements from the same day as depicted in Fig. 19a (Frieß et al., 2011). Despite one outlier retrieved from

Tropospheric BrO in the Arctic: satellite retrieval and ground-based data

H. Sihler et al.

Title Page

Abstract

Introduction

Conclusions

References

Tables

Figures

⏪

⏩

◀

▶

Back

Close

Full Screen / Esc

Printer-friendly Version

Interactive Discussion



measurements around 11:30 AST, all retrieved profiles feature a positive BrO gradient close to the surface. However, most BrO is still located within the boundary layer.

From the data presented in this study, we conclude that events of enhanced BrO are well captured by satellite measurements, and that ground-based observation and tropospheric VCDs retrieved from GOME-2 data are significantly correlated. The surface-near concentrations measured by LP-DOAS furthermore indicate, that the satellite observations in turn are linked to surface processes as observed from aboard the Amundsen. At Barrow, however, deviations from this general dependence could be explained by local meteorological perturbations and variations of the surface BrO column height. Occasionally, satellite measurements may underestimate the influence by bromine activation when the surface BrO layer is extremely shallow and horizontal gradients of both the chemistry and the surface sensitivity are large. The general applicability of this observation, however, needs to be tested further because the presented study comprises only a relatively small number of ground-based observations over the sea-ice.

5 Conclusions

We present a new algorithm to retrieve residual tropospheric columns of Arctic BrO solely based on data from a single satellite instrument. Two important properties of our algorithm are that it identifies measurements (a) with significantly enhanced tropospheric BrO amounts which can not be explained by stratospheric processes and (b) which are sensitive for near-surface layers. Unlike earlier attempts to solve this task, the presented approach does not depend on extensive chemistry models and climatological data. Only potential vorticity fields are supplied from external sources allowing to identify the polar vortex, where the retrieval algorithm is not applicable. This procedure is necessary to provide a consistent data-set without artefacts caused by a disturbed stratospheric chemistry. Based on this work, possible surface processes involved in Arctic bromine activation can be studied.

Tropospheric BrO in the Arctic: satellite retrieval and ground-based data

H. Sihler et al.

Title Page

Abstract

Introduction

Conclusions

References

Tables

Figures

⏪

⏩

◀

▶

Back

Close

Full Screen / Esc

Printer-friendly Version

Interactive Discussion



distributed over the entire instrument swath. In the ϑ and V_N -direction, however, a partitioning algorithm accounting for non-uniform distributions is required. Partitions all containing a similar number of observations is desirable in order to achieve a homogeneous statistics of the asymmetry filter applied on every partition separately.

The two dimensional partitioning algorithm applied on each ψ -bin is based on a partition of Ω which can be indexed by two indices i, j for the ϑ and V_N -direction, respectively:

$$\Omega_\beta = \Omega_{i,j}. \quad (\text{A1})$$

The necessary steps are explained by means of a concrete example.

In order to sample the \bar{z} -surface in the two dimensions of the (ϑ, V_N) -plane, T is subdivided into N_ϑ times N_V partitions $\Omega_{i,j} \subset \Omega$ with $i = 1, \dots, N_\vartheta$ and $j = 1, \dots, N_V$, respectively. The partitioning is performed on the two-dimensional domain Ω

$$\Omega = [25^\circ, 80^\circ] \times [0, 8 \times 10^{15} \text{ molec cm}^{-2}] \quad (\text{A2})$$

encompassing the SZA interval between 25° and 80° and the NO_2 VCD interval between 0 and $8 \times 10^{15} \text{ molec cm}^{-2}$, respectively. The partitioning is first initialized and then iteratively optimized until each partition contains an almost equally large subset of T .

The partitioning of Ω is initialized in two steps. Figure A1 shows an example of this procedure performed on Ω for 25 March 2009. (1) T is divided into N_ϑ preliminary partitions along the ϑ -axis each containing an equal number of observations except the last two columns ($i = N_\vartheta - 1, N_\vartheta$) whose size is weighted by two in order to allow for a higher density of bins at this edge of the domain. The borders between the partitions are denoted h_i ($i = 1, \dots, N_\vartheta - 1$) in Fig. A1. (2) Subsequently, the preliminary partitioning nodes defining the boundaries of each partition in V_N -direction are calculated. For each $i = 1, \dots, N_\vartheta - 1$, we construct a set union T_i

$$T_i = \bigcup_{j=1}^{N_V} T_{i,j} \bigcup_{j=1}^{N_V} T_{i+1,j} \quad (\text{A3})$$

Tropospheric BrO in the Arctic: satellite retrieval and ground-based data

H. Sihler et al.

Title Page

Abstract

Introduction

Conclusions

References

Tables

Figures

◀

▶

◀

▶

Back

Close

Full Screen / Esc

Printer-friendly Version

Interactive Discussion



Tropospheric BrO in the Arctic: satellite retrieval and ground-based data

H. Sihler et al.

Title Page

Abstract

Introduction

Conclusions

References

Tables

Figures

⏪

⏩

◀

▶

Back

Close

Full Screen / Esc

Printer-friendly Version

Interactive Discussion



containing all observations in the column left and right of the respective h_i . Each T_j is then divided into N_V partitions in V_N -direction defining the (ϑ, V_N) -coordinates of the preliminary partitioning nodes. This time, however, the first and last partition (top and bottom row) contain only half as many observation compared to the six partitions in between. The modification to the basic scheme of partitions containing an equal number of measurements prevents the outer partitions from becoming too large on the cost of retrieval noise. Finally, this procedure leads to a total of $N_\vartheta \times N_V$ initial partitioning nodes defining the boundaries of the partitions as depicted in Fig. A1.

After computing the initial coordinates of the partitioning nodes, the coordinates of the nodes are iteratively fine-tuned until all partitions contain an almost equal number of measurements. The fine-tuning is first performed for the node in the bottom left of Fig. A1 and then consecutively followed by the nodes to the right and then line-by-line upward. The fine-tuning is implemented as follows: It is tested how the variance of the number of measurements in the adjacent partitions behaves when the position of the actual boundary slightly changes. The node is consecutively displaced horizontally by $\pm\Delta\vartheta$ and vertically by $\pm\Delta V_N$. If the variance at one of the four positions is smaller than at the old position, the new position with the minimum variance is chosen as the new position and the procedure is repeated in the neighbourhood of the new position. The fine-tuning of each node is repeated up to five times before moving on to the next node. $\Delta\vartheta$ and ΔV_N depend on the minimum distance to neighbouring nodes in the respective direction and decrease in each iteration.

In order to finalize the partitioning algorithm, the number of measurements in all partitions is computed after all nodes have been fine-tuned separately. The fine-tuning algorithm is terminated when the number variation is less than 20 % (the first and last row of partitions $T_{i,j}$ for $i = V_\vartheta$ and $j = 1, V_N$ are treated differently as described above). Otherwise the fine-tuning is repeated for all nodes until the 20 %-criterion is reached. Usually, the algorithm converges after 5 repetitions or less. Figure 4 illustrates the final partitioning of Ω . Numerical inspection presented in Sect. 3.1 revealed that a value of

$N_{\theta} = 5$ and $N_{\psi} = N_V = 8$ lead to sufficiently accurate results. The limits of the bins in ψ -direction are fixed to $\pm 14^{\circ}$ and $\pm 34^{\circ}$, respectively.

Supplementary material related to this article is available online at:

<http://www.atmos-meas-tech-discuss.net/5/3199/2012/>

[amtd-5-3199-2012-supplement.pdf](#).

Acknowledgements. Inspiring discussions with the following individuals during the preparation of this work is heartily acknowledged: N. Theys (IASB/BIRA), J. Buxmann (IUP Heidelberg), G. Ziegler (Uni Jena), L. Kaleschke (Uni Hamburg), and J. Ström (Uni Tromsø). For their technical support R. Sörensen and K. Mies at MPIC are acknowledged. AMSR-E sea-ice concentration maps have been provided by the ICDC, KlimaCampus Hamburg. M. Van Roozendaal and C. Fayt from IASB/BIRA are acknowledged for providing the WinDOAS software. GOME-2 and AVHRR level-1 data have been provided by EUMETSAT. ECMWF operational data have been obtained from the ECMWF Data Server. CALIPSO data has been obtained from the NASA Langley Research Center Atmospheric Science Data Center. The ozone profile was provided by NOAA Earth System Research Laboratory (ESRL, <http://www.esrl.noaa.gov/gmd/obop/brw>). This work has been financially supported by the German Research Association (FR2497/2-1 and PL193/10-1) and the International Max Planck Research School for Atmospheric Chemistry and Physics, Mainz (Germany).

The service charges for this open access publication have been covered by the Max Planck Society.

Tropospheric BrO in the Arctic: satellite retrieval and ground-based data

H. Sihler et al.

Title Page

Abstract

Introduction

Conclusions

References

Tables

Figures



Back

Close

Full Screen / Esc

Printer-friendly Version

Interactive Discussion



References

- Acarreta, J. R., De Haan, J. F., and Stammes, P.: Cloud pressure retrieval using the O₂-O₂ absorption band at 477 nm, *J. Geophys. Res.*, 109, D05204, doi:10.1029/2003JD003915, 2004. 3203
- 5 Afe, O., Richter, A., Sierk, B., Wittrock, F., and Burrows, J.: BrO emission from volcanoes: a survey using GOME and SCIAMACHY measurements, *Geophys. Res. Lett.*, 31, L24113, doi:10.1029/2004GL020994, 2004. 3205
- Aliwell, S. R., Van Roozendaal, M., Johnston, P. V., Richter, A., Wagner, T., Arlander, D. W., Burrows, J. P., Fish, D. J., Jones, R. L., Tørnkvist, K. K., Lambert, J.-C., Pfeilsticker, K., and
10 Pundt, I.: Analysis for BrO in zenith-sky spectra: an intercomparison exercise for analysis improvement, *J. Geophys. Res.*, 107, D14, doi:10.1029/2001JD000329, 2002. 3205
- Atkinson, R., Baulch, D. L., Cox, R. A., Crowley, J. N., Hampson, R. F., Hynes, R. G., Jenkin, M. E., Rossi, M. J., and Troe, J.: Evaluated kinetic and photochemical data for atmospheric chemistry: Volume III – gas phase reactions of inorganic halogens, *Atmos. Chem. Phys.*, 7, 981–1191, doi:10.5194/acp-7-981-2007, 2007. 3208
- 15 Barrie, L. A., Bottenheim, J. W., Schnell, R. C., Crutzen, P. J., and Rasmussen, R.: Ozone destruction and photochemical reactions at polar sunrise in the lower Arctic atmosphere, *Nature*, 334, 138–141, 1988. 3200
- Begoin, M., Richter, A., Weber, M., Kaleschke, L., Tian-Kunze, X., Stohl, A., Theys, N., and Burrows, J. P.: Satellite observations of long range transport of a large BrO plume in the Arctic, *Atmos. Chem. Phys.*, 10, 6515–6526, doi:10.5194/acp-10-6515-2010, 2010. 3202
- 20 Bogumil, K., Orphal, J., Homann, T., Voigt, S., Spietz, P., and Fleischmann, O.: Measurements of molecular absorption spectra with the SCIAMACHY pre-flight model: instrument characterization and reference data for atmospheric remote-sensing in the 230–2380 nm region, *J. Photoch. Photobio. A*, 157, 167–184, doi:10.1016/S1010-6030(03)00062-5, 2003. 3247
- 25 Burrows, J., Dehn, A., Deters, B., Himmelmann, S., Richter, A., and Voigt, S.: Atmospheric remote-sensing reference data from GOME: Part 1. Temperature-dependent absorption cross-sections of NO₂ in the 231–794 nm range, *J. Quant. Spectrosc. Ra.*, 60, 1025–1031, doi:10.1016/S0022-4073(97)00197-0, 1998. 3247
- 30 Callies, J., Corpaccioli, E., Eisinger, M., Hahne, A., and Lefebvre, A.: GOME-2 – MetOp's second-generation sensor for operational ozone monitoring, *ESA Bull.*, 102, 28–36, 2000. 3203

Tropospheric BrO in the Arctic: satellite retrieval and ground-based data

H. Sihler et al.

Title Page

Abstract

Introduction

Conclusions

References

Tables

Figures

⏪

⏩

◀

▶

Back

Close

Full Screen / Esc

Printer-friendly Version

Interactive Discussion



Tropospheric BrO in the Arctic: satellite retrieval and ground-based data

H. Sihler et al.

Title Page

Abstract

Introduction

Conclusions

References

Tables

Figures

◀

▶

◀

▶

Back

Close

Full Screen / Esc

Printer-friendly Version

Interactive Discussion



Cantrell, C. A.: Technical Note: Review of methods for linear least-squares fitting of data and application to atmospheric chemistry problems, *Atmos. Chem. Phys.*, 8, 5477–5487, doi:10.5194/acp-8-5477-2008, 2008. 3229

Chance, K.: Analysis of BrO measurements from the global ozone monitoring experiment, *Geophys. Res. Lett.*, 25, 3335–3338, doi:10.1029/98GL52359, 1998. 3201

Choi, S., Wang, Y., Salawitch, R. J., Canty, T., Joiner, J., Zeng, T., Kurosu, T. P., Chance, K., Richter, A., Huey, L. G., Liao, J., Neuman, J. A., Nowak, J. B., Dibb, J. E., Weinheimer, A. J., Diskin, G., Ryerson, T. B., da Silva, A., Curry, J., Kinnison, D., Tilmes, S., and Levelt, P. F.: Analysis of satellite-derived Arctic tropospheric BrO columns in conjunction with aircraft measurements during ARCTAS and ARCPAC, *Atmos. Chem. Phys.*, 12, 1255–1285, doi:10.5194/acp-12-1255-2012, 2012. 3201, 3202

Clémer, K., Van Roozendael, M., Fayt, C., Hendrick, F., Hermans, C., Pinardi, G., Spurr, R., Wang, P., and De Mazière, M.: Multiple wavelength retrieval of tropospheric aerosol optical properties from MAXDOAS measurements in Beijing, *Atmos. Meas. Tech.*, 3, 863–878, doi:10.5194/amt-3-863-2010, 2010. 3216

De Smedt, I., Van Roozendael, M., and Jacobs, T.: Optimization of DOAS settings for BrO fitting from SCIAMACHY nadir spectra – comparison with GOME BrO retrievals, Tech. rep., Belg. Inst. for Space Aeron., Brussels, Belgium, available at: <http://bro.aeronomie.be/BIRA-SCIABrO.pdf> (last access: 2 May 2012), 2004. 3205

Deutschmann, T., Beirle, S., Frieß, U., Grzegorski, M., Kern, C., Kritten, L., Platt, U., Prados-Román, C., Pukite, J., Wagner, T., Werner, B., and Pfeilsticker, K.: The Monte Carlo atmospheric radiative transfer model McArtim: introduction and validation of Jacobians and 3-D features, *J. Quant. Spectrosc. Ra.*, 112, 1119–1137, doi:10.1016/j.jqsrt.2010.12.009, 2011. 3217

Dorf, M., Butler, J. H., Butz, A., Camy-Peyret, C., Chipperfield, M. P., Kritten, L., Montzka, S. A., Simmes, B., Weidner, F., and Pfeilsticker, K.: Long-term observations of stratospheric bromine reveal slow down in growth, *Geophys. Res. Lett.*, 33, L24808, doi:10.1029/2006GL027714, 2006. 3208

Frieß, U., Sihler, H., Sander, R., Pöhler, D., Yilmaz, S., and Platt, U.: The vertical distribution of BrO and aerosols in the Arctic: measurements by active and passive differential optical absorption spectroscopy, *J. Geophys. Res.*, 116, D00R04, doi:10.1029/2011JD015938, 2011. 3201, 3215, 3228, 3232, 3233, 3269

Tropospheric BrO in the Arctic: satellite retrieval and ground-based data

H. Sihler et al.

Title Page

Abstract

Introduction

Conclusions

References

Tables

Figures

⏪

⏩

◀

▶

Back

Close

Full Screen / Esc

Printer-friendly Version

Interactive Discussion



- Kaleschke, L., Richter, A., Burrows, J., Afe, O., Heygster, G., Notholt, J., Rankin, A. M., Roscoe, H. K., Hollwedel, J., Wagner, T., and Jacobi, H.-W.: Frost flowers on sea ice as a source of sea salt and their influence on tropospheric halogen chemistry, *Geophys. Res. Let.*, 31, L16114, doi:10.1029/2004GL020655, 2004. 3201
- 5 King, M. D.: Determination of the scaled optical thickness of clouds from reflected solar radiation measurements, *J. Atmos. Sci.*, 44, 1734–1751, doi:10.1175/1520-0469(1987)044<1734:DOTSOT>2.0.CO;2, 1987. 3218
- Kraus, S.: DOASIS: DOAS Intelligent System, Software, copyright 2004 Stefan Kraus, Institute of Environmental Physics, University of Heidelberg, in cooperation with Hoffmann Messtechnik GmbH, Heidelberg, 2004. 3205
- 10 Liao, J., Sihler, H., Huey, L., Neuman, J., Tanner, D., Friess, U., Platt, U., Flocke, F. M., Orlando, J. J., Shepson, P. B., Beine, H. J., Weinheimer, A. J., Sjostedt, S. J., Nowak, J. B., Knapp, D. J., Staebler, R. M., Zheng, W., Sander, R., Hall, S. R., and Ullmann, K.: A comparison of Arctic BrO measurements by chemical ionization mass spectrometry and long path-differential optical absorption spectroscopy, *J. Geophys. Res.*, 116, D00R02, doi:10.1029/2010JD014788, 2011. 3201, 3228, 3231, 3232
- 15 Martin, R. V., Chance, K., Jacob, D., Kurosu, T. P., Spurr, R. J. D., Bucsela, E., Gleason, J. F., Palmer, P. I., Bey, I., Fiore, A. M., Li, Q., Yantosca, R. M., and Koelemeijer, R. B. A.: An improved retrieval of tropospheric nitrogen dioxide from GOME, *J. Geophys. Res.*, 107, 4437, doi:10.1029/2001JD001027, 2002. 3218
- 20 Munro, R., Eisinger, M., Anderson, C., Callies, J., Corpaccioli, E., Lang, R., Lefebvre, A., Livschitz, Y., and Albiñana, A. P.: GOME-2 on MetOp, in: Proc. of The 2006 EUMETSAT Meteorological Satellite Conference, Helsinki, Finland, 12–16 June 2006, N/A ISBN 92-9110-076-5, EUMETSAT, 48, 2006. 3203
- 25 NASA: CloudSat-CALIPSO Launch, Press kit, National Aeronautics and Space Administration, http://www.jpl.nasa.gov/news/press_kits/cloudsat-calipso-launch.pdf (last access: 2 May 2011), 2006. 3225
- O’Byrne, G., Martin, R. V., van Donkelaar, A., Joiner, J., and Celarier, E. A.: Surface reflectivity from the ozone monitoring instrument using the moderate resolution imaging spectroradiometer to eliminate clouds: effects of snow on ultraviolet and visible trace gas retrievals, *J. Geophys. Res.*, 115, D17305, doi:10.1029/2009JD013079, 2010. 3203
- 30 Platt, U. and Stutz, J.: Differential Optical Absorption Spectroscopy (DOAS) – Principles and Applications, Springer-Verlag, Berlin, Heidelberg, 2008. 3201, 3205

Tropospheric BrO in the Arctic: satellite retrieval and ground-based data

H. Sihler et al.

Title Page

Abstract

Introduction

Conclusions

References

Tables

Figures

◀

▶

◀

▶

Back

Close

Full Screen / Esc

Printer-friendly Version

Interactive Discussion



- Pöhler, D., Vogel, L., Frieß, U., and Platt, U.: Observation of halogen species in the Amundsen Gulf, Arctic, by active long-path differential optical absorption spectroscopy, *P. Natl. Acad. Sci. USA*, 107, 6582–6587, doi:10.1073/pnas.0912231107, 2010. 3201, 3215, 3227, 3231
- Prados-Roman, C., Butz, A., Deutschmann, T., Dorf, M., Kritten, L., Minikin, A., Platt, U., Schlager, H., Sihler, H., Theys, N., Van Roozendael, M., Wagner, T., and Pfeilsticker, K.: Airborne DOAS limb measurements of tropospheric trace gas profiles: case studies on the profile retrieval of O₄ and BrO, *Atmos. Meas. Tech.*, 4, 1241–1260, doi:10.5194/amt-4-1241-2011, 2011. 3215, 3222, 3227
- Press, W. H., Teukolsky, S. A., Vetterling, W. T., and Flannery, B. P.: *Numerical Recipes in C++*, 3rd Edn., Cambridge University Press, Cambridge, New York, 2007. 3211
- Quarteroni, A., Sacco, R., and Saleri, F.: *Numerische Mathematik 2*, Springer Verlag, Berlin Heidelberg, 2002. 3211
- Richter, A., Wittrock, F., Eisinger, M., and Burrows, J.: GOME observations of tropospheric BrO in northern hemispheric spring and summer 1997, *Geophys. Res. Lett.*, 25, 2683–2686, doi:10.1029/98GL52016, 1998. 3201
- Richter, A., Wittrock, F., Ladstätter-Weissenmayer, A., and Burrows, J. P.: GOME measurements of stratospheric and tropospheric BrO, *Adv. Space Res.*, 29, 1667–1672, doi:10.1016/S0273-1177(02)00123-0, 2002. 3201, 3210
- Rothman, L., Gamache, R., Tipping, R., Rinsland, C., Smith, M., and Benner, D.: The HITRAN molecular database – editions of 1991 and 1992, *J. Quant. Spectrosc. Ra.*, 48, 469–507, 1992. 3247
- Salawitch, R. J., Canty, T., Kurosu, T., Chance, K., Liang, Q., da Silva, A., Pawson, S., Nielsen, J. E., Rodriguez, J. M., Bhartia, P. K., Liu, X., Huey, L. G., Liao, J., Stickel, R. E., Tanner, D. J., Dibb, J. E., Simpson, W. R., Donohoue, D., Weinheimer, A., Flocke, F., Knapp, D., Montzka, D., Neuman, J. A., Nowak, J. B., Ryerson, T. B., Oltmans, S., Blake, D. R., Atlas, E. L., Kinnison, D. E., Tilmes, S., Pan, L. L., Hendrick, F., Van Roozendael, M., Kreher, K., Johnston, P. V., Gao, R. S., Johnson, B., Bui, T. P., Chen, G., Pierce, R. B., Crawford, J. H., Jacob, D. J.: A new interpretation of total column BrO during arctic spring, *Geophys. Res. Lett.*, 37, L21805, doi:10.1029/2010GL043798, 2010. 3201, 3202, 3208
- Seabrook, J. A., Whiteway, J., Staebler, R. M., Bottenheim, J. W., Komguem, L., Gray, L. H., Barber, D., and Asplin, M.: LIDAR measurements of Arctic boundary layer ozone depletion events over the frozen Arctic Ocean, *J. Geophys. Res.*, 116, D00S02, doi:10.1029/2011JD016335, 2011. 3232

Tropospheric BrO in the Arctic: satellite retrieval and ground-based data

H. Sihler et al.

[Title Page](#)[Abstract](#)[Introduction](#)[Conclusions](#)[References](#)[Tables](#)[Figures](#)[◀](#)[▶](#)[◀](#)[▶](#)[Back](#)[Close](#)[Full Screen / Esc](#)[Printer-friendly Version](#)[Interactive Discussion](#)

- Simpson, W. R., von Glasow, R., Riedel, K., Anderson, P., Ariya, P., Bottenheim, J., Burrows, J., Carpenter, L. J., Frieß, U., Goodsite, M. E., Heard, D., Hutterli, M., Jacobi, H.-W., Kaleschke, L., Neff, B., Plane, J., Platt, U., Richter, A., Roscoe, H., Sander, R., Shepson, P., Sodeau, J., Steffen, A., Wagner, T., and Wolff, E.: Halogens and their role in polar boundary-layer ozone depletion, *Atmos. Chem. Phys.*, 7, 4375–4418, doi:10.5194/acp-7-4375-2007, 2007. 3201
- Sinnhuber, B.-M., Arlander, D. W., Bovensmann, H., Burrows, J. P., Chipperfield, M. P., Enell, C.-F., Frieß, U., Hendrick, F., Johnston, P. V., Jones, R. L., Kreher, K., Mohamed-Tahrin, N., Müller, R., Pfeilsticker, K., Platt, U., Pommereau, J.-P., Pundt, I., Richter, A., South, A. M., Tørnkvist, K. K., Van Roozendaal, M., Wagner, T., and Wittrock, F.: Comparison of measurements and model calculations of stratospheric bromine monoxide, *J. Geophys. Res.-Biogeo.*, 107, 4398, doi:10.1029/2001JD000940, 2002. 3208
- Spreen, G., Kaleschke, L., and Heygster, G.: Sea ice remote sensing using AMSR-E 89-GHz channels, *J. Geophys. Res.-Biogeo.*, 113, C02S03, doi:10.1029/2005JC003384, 2008. 3226
- Stutz, J. and Platt, U.: Numerical analysis and estimation of the statistical error of differential optical absorption spectroscopy measurements with least-squares methods, *Appl. Optics*, 35, 6041–6053, doi:10.1364/AO.35.006041, 1996. 3221
- Theys, N., Van Roozendaal, M., Errera, Q., Hendrick, F., Daerden, F., Chabrilat, S., Dorf, M., Pfeilsticker, K., Rozanov, A., Lotz, W., Burrows, J. P., Lambert, J.-C., Goutail, F., Roscoe, H. K., and De Mazière, M.: A global stratospheric bromine monoxide climatology based on the BASCOE chemical transport model, *Atmos. Chem. Phys.*, 9, 831–848, doi:10.5194/acp-9-831-2009, 2009. 3201, 3202, 3208
- Theys, N., Van Roozendaal, M., Hendrick, F., Yang, X., De Smedt, I., Richter, A., Begoin, M., Errera, Q., Johnston, P. V., Kreher, K., and De Mazière, M.: Global observations of tropospheric BrO columns using GOME-2 satellite data, *Atmos. Chem. Phys.*, 11, 1791–1811, doi:10.5194/acp-11-1791-2011, 2011. 3202, 3227
- Toyota, K., McConnell, J. C., Lupu, A., Neary, L., McLinden, C. A., Richter, A., Kwok, R., Semeniuk, K., Kaminski, J. W., Gong, S.-L., Jarosz, J., Chipperfield, M. P., and Sioris, C. E.: Analysis of reactive bromine production and ozone depletion in the Arctic boundary layer using 3-D simulations with GEM-AQ: inference from synoptic-scale patterns, *Atmos. Chem. Phys.*, 11, 3949–3979, doi:10.5194/acp-11-3949-2011, 2011. 3202

Tropospheric BrO in the Arctic: satellite retrieval and ground-based data

H. Sihler et al.

[Title Page](#)[Abstract](#)[Introduction](#)[Conclusions](#)[References](#)[Tables](#)[Figures](#)[⏪](#)[⏩](#)[◀](#)[▶](#)[Back](#)[Close](#)[Full Screen / Esc](#)[Printer-friendly Version](#)[Interactive Discussion](#)

Tuckermann, M., Ackermann, R., Golz, C., Lorenzen-Schmidt, H., Senne, T., Stutz, J., Trost, B., Unold, W., and Platt, U.: DOAS-observation of halogen radical-catalysed arctic boundary layer ozone destruction during the ARCTOC-campaigns 1995 and 1996 in Ny-Alesund, Spitsbergen, *Tellus B*, 49, 533–555, 1997. 3201

5 Vandaele, A., Hermans, C., Simon, P., Carleer, M., Colin, R., and Fally, S.: Measurements of the NO₂ absorption cross-section from 42 000 cm⁻¹ to 10 000 cm⁻¹ (238–1000 nm) at 220 K and 294 K, *J. Quant. Spectrosc. Ra.*, 59, 171–184, doi:10.1016/S0022-4073(97)00168-4, 1998. 3247

10 Vasilkov, A. P., Joiner, J., Haffner, D., Bhartia, P. K., and Spurr, R. J. D.: What do satellite backscatter ultraviolet and visible spectrometers see over snow and ice? A study of clouds and ozone using the A-train, *Atmos. Meas. Tech.*, 3, 619–629, doi:10.5194/amt-3-619-2010, 2010. 3203, 3215

Volkamer, R., Spietz, P., Burrows, J., and Platt, U.: High-resolution absorption cross-section of glyoxal in the UV-vis and IR spectral ranges, *J. Photochem. Photobio. A*, 172, 35–46, doi:10.1016/j.jphotochem.2004.11.011, 2005. 3247

15 Wagner, T.: Satellite Observations of Atmospheric Halogen Oxides, Ph.D. thesis, University of Heidelberg, Mensch & Buch Verlag, Berlin, 1999. 3201

Wagner, T. and Platt, U.: Satellite mapping of enhanced BrO concentrations in the troposphere, *Nature*, 395, 486–490, doi:10.1038/26723, 1998. 3201, 3205, 3214

20 Wagner, T., Leue, C., Wenig, M., Pfeilsticker, K., and Platt, U.: Spatial and temporal distribution of enhanced boundary layer BrO concentrations measured by the GOME instrument aboard ERS-2, *J. Geophys. Res.*, 106, 24225–24235, 2001. 3201

25 Wagner, T., Ibrahim, O., Sinreich, R., Frieß, U., von Glasow, R., and Platt, U.: Enhanced tropospheric BrO over Antarctic sea ice in mid winter observed by MAX-DOAS on board the research vessel Polarstern, *Atmos. Chem. Phys.*, 7, 3129–3142, doi:10.5194/acp-7-3129-2007, 2007. 3201, 3215, 3233

Wagner, T., Beirle, S., and Deutschmann, T.: Three-dimensional simulation of the Ring effect in observations of scattered sun light using Monte Carlo radiative transfer models, *Atmos. Meas. Tech.*, 2, 113–124, doi:10.5194/amt-2-113-2009, 2009a. 3205

30 Wagner, T., Deutschmann, T., and Platt, U.: Determination of aerosol properties from MAX-DOAS observations of the Ring effect, *Atmos. Meas. Tech.*, 2, 495–512, doi:10.5194/amt-2-495-2009, 2009b. 3216

Tropospheric BrO in the Arctic: satellite retrieval and ground-based data

H. Sihler et al.

[Title Page](#)[Abstract](#)[Introduction](#)[Conclusions](#)[References](#)[Tables](#)[Figures](#)[⏪](#)[⏩](#)[◀](#)[▶](#)[Back](#)[Close](#)[Full Screen / Esc](#)[Printer-friendly Version](#)[Interactive Discussion](#)

Wang, P., Stammes, P., van der A, R., Pinardi, G., and Van Roozendael, M.: FRESCO+: an improved O₂ A-band cloud retrieval algorithm for tropospheric trace gas retrievals, *Atmos. Chem. Phys.*, 8, 6565–6576, doi:10.5194/acp-8-6565-2008, 2008. 3203

Wilmouth, D., Hanisco, T., Donahue, N., and Anderson, J.: Fourier transform ultraviolet spectroscopy of the A²Π_(3/2) ← X²Π_(3/2) transition of BrO, *J. Phys. Chem. A*, 103, 8935–8945, doi:10.1021/jp991651o, 1999. 3247

Winker, D. M., Hunt, W. H., and McGill, M. J.: Initial performance assessment of CALIOP, *Geophys. Res. Lett.*, 34, L19803, doi:10.1029/2007GL030135, 2007. 3225

Tropospheric BrO in the Arctic: satellite retrieval and ground-based data

H. Sihler et al.

Title Page

Abstract

Introduction

Conclusions

References

Tables

Figures

◀

▶

◀

▶

Back

Close

Full Screen / Esc

Printer-friendly Version

Interactive Discussion



Table 1. Compilation of fit ranges, reference cross-sections and parameters of the three DOAS evaluations of calibrated radiance spectra measured by GOME-2. The slant column densities (SCDs) of BrO, O₃, O₄ and NO₂ are retrieved. The synthetic Ring spectra account for (wavelength-dependent) inelastic Raman scattering and the reciprocal intensity spectrum accounts for instrumental stray-light (see text). The fit-polynomial models broadband absorption.

Retrieved SCD	BrO and O ₃	O ₄	NO ₂
GOME-2 band	2B	2B	4
Pixel number	301–503	459–759	185–288
Wavelength (nm)	336–360	355–390	431–453
O ₃ (243 K)	Gür et al. (2005)	*	–
O ₃ (223 K)	Gür et al. (2005)	–	–
O ₃ (221 K)	–	–	Burrows et al. (1998)
BrO (228 K)	Wilmouth et al. (1999)	–	–
O ₄	Greenblatt et al. (1990)	*	*
NO ₂ (220 K)	Vandaele et al. (1998)	*	*
OCIO (293 K)	Bogumil et al. (2003)	–	–
SO ₂ (273 K)	Bogumil et al. (2003)	–	–
H ₂ O (300 K)	–	–	Rothman et al. (1992)
CHOCHO	–	–	Volkamer et al. (2005)
Ring×λ ⁴	yes	yes	no
Ring (norm)	yes	yes	yes
Reciprocal	yes	yes	no
Polynomial	4th order	3rd order	4th order

The asterisk (*) denotes that the reference in the column to the left is applied.

Tropospheric BrO in the Arctic: satellite retrieval and ground-based data

H. Sihler et al.

Table 2. Summary of all modelled geometries for which the threshold parametrization is performed. The solar zenith angle (SZA), relative azimuth angle (RAA), and viewing zenith angle (VZA) are defined in the satellite system, respectively.

Parameter	Node
SZA (°)	28, 44, 56, 64, 66, 68, 72, 76, 80, 82, 84, 86
RAA (°)	0, 20, 32, 36, 44, 48, 52, 56, 60, 64, 116, 120, 124, 128, 132, 136, 144, 148, 160, 180
VZA (°)	0 (nadir), 16, 32, 48
Elev. (km)	0, 1, 2, 3, 4, 5, 6

Title Page

Abstract

Introduction

Conclusions

References

Tables

Figures

◀

▶

◀

▶

Back

Close

Full Screen / Esc

Printer-friendly Version

Interactive Discussion

Tropospheric BrO in the Arctic: satellite retrieval and ground-based data

H. Sihler et al.

Table 3. Modelled layers of scattering media (aerosols and/or clouds) defined by their lower and upper edge over ground and the optical density (OD).

Layer (km)	OD
0–1	1, 3, 10, 20, 50
1–2	1, 3, 10, 50
3–4	50
7–8	1, 3, 10, 50

[Title Page](#)[Abstract](#)[Introduction](#)[Conclusions](#)[References](#)[Tables](#)[Figures](#)[◀](#)[▶](#)[◀](#)[▶](#)[Back](#)[Close](#)[Full Screen / Esc](#)[Printer-friendly Version](#)[Interactive Discussion](#)

Tropospheric BrO in the Arctic: satellite retrieval and ground-based data

H. Sihler et al.

Table 4. Differences between CALIOP/CALIPSO and the GOME-2/MetOp-A.

	CALIOP/CALIPSO	GOME-2/MetOp-A
Footprint	70 m diameter	80 × 40 km ²
Swath-width	–	1920 km
Equator crossing	13:30 LT	09:30 LT
Flight altitude	705 km	817 km
Orbital period	99 min	101 min
Inclination	98.2°	98.7°

Title Page

Abstract

Introduction

Conclusions

References

Tables

Figures

◀

▶

◀

▶

Back

Close

Full Screen / Esc

Printer-friendly Version

Interactive Discussion



Tropospheric BrO in the Arctic: satellite retrieval and ground-based data

H. Sihler et al.

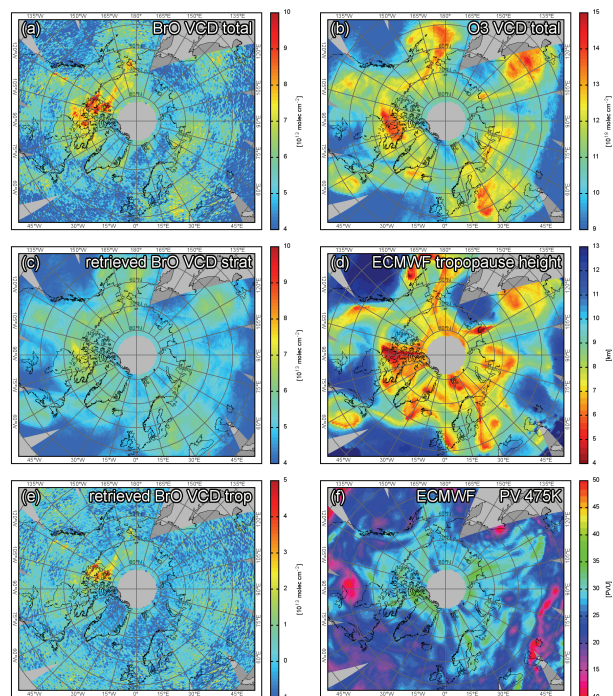


Fig. 1. Illustration of the decomposition of the total BrO VCD measured by GOME-2 into stratospheric and tropospheric contribution for 25 March 2009. The top row shows VCDs of BrO **(a)** and O₃ **(b)** assuming a geometric AMF. Coinciding spatial structures of enhanced VCDs are visible e.g. over Eastern Europe and Northern Siberia, which are attributed to stratospheric dynamics and variations of the tropopause height **(d)**. The BrO SCD_{strat} **(c)** is retrieved from measurements of BrO, O₃, and NO₂ alone. The BrO VCD_{trop} **(e)** is the difference between **(a)** and **(c)**. The PV at the 475K isentropic **(f)** may be used to identify regions within the polar vortex (see Sect. 2.2.2). All VCDs are calculated using a geometric AMF, gray areas contain no data.

Title Page

Abstract

Introduction

Conclusions

References

Tables

Figures

◀

▶

◀

▶

Back

Close

Full Screen / Esc

Printer-friendly Version

Interactive Discussion

Tropospheric BrO in the Arctic: satellite retrieval and ground-based data

H. Sihler et al.

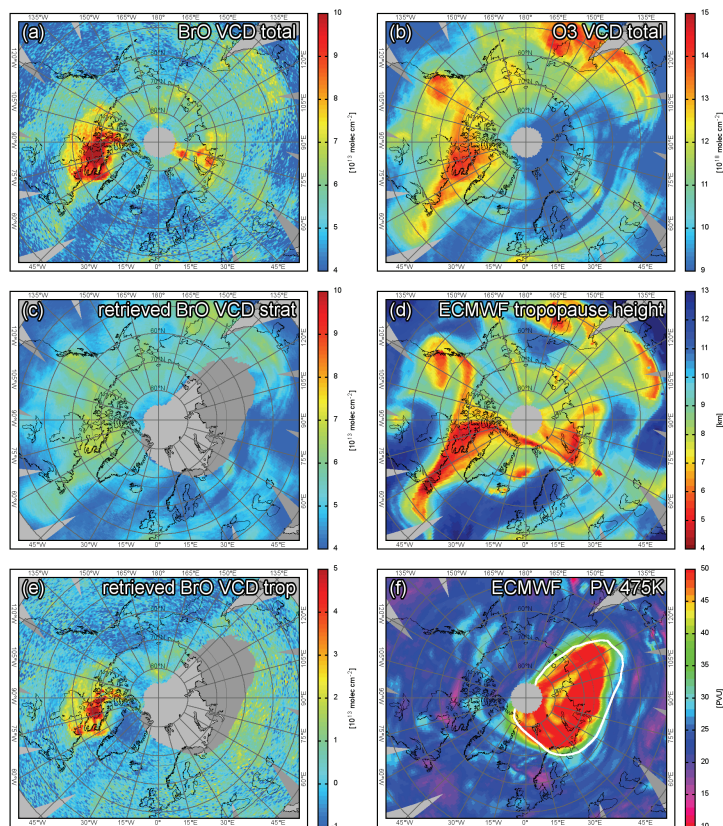


Fig. 2. Same as in Fig. 1, but for 1 April 2007. The white contour in **(f)** marks the 75 PVU-isoline at the 550 K isentropic surface. The decomposition into stratospheric and tropospheric column fails within the polar vortex, because there is no clear correlation between O₃ VCD and the tropopause height **(d)** any more.

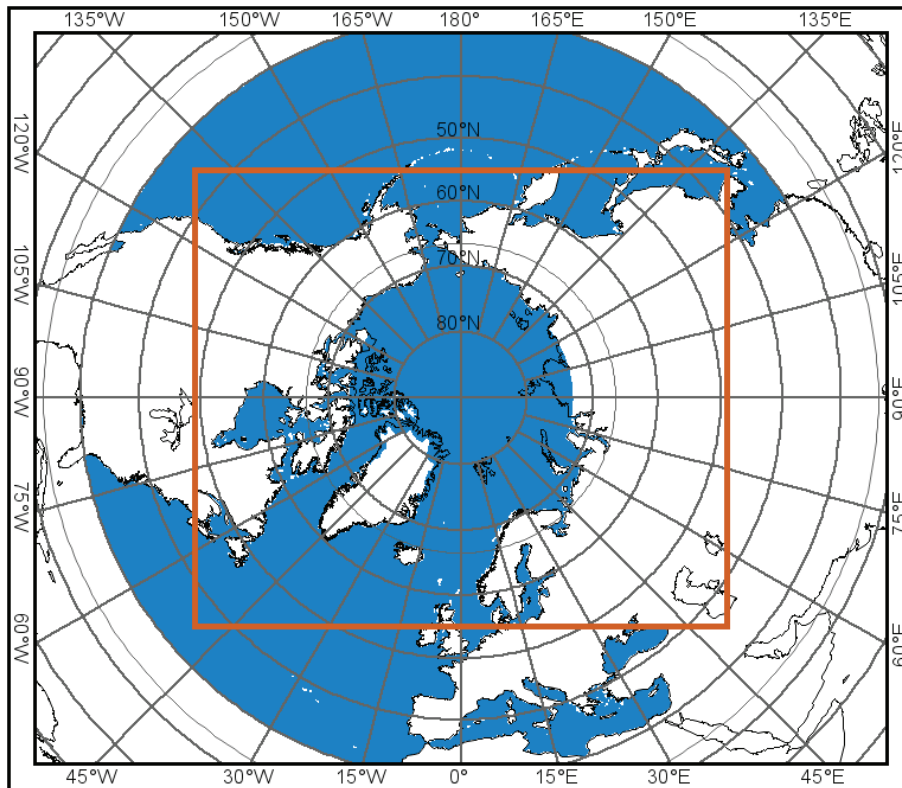


Fig. 3. Map of the geographical area encompassing the reference measurements used to estimate the stratospheric BrO column highlighted in blue. The orange rectangle denotes the limits of the other maps in this paper.

Tropospheric BrO in the Arctic: satellite retrieval and ground-based data

H. Sihler et al.

Title Page	
Abstract	Introduction
Conclusions	References
Tables	Figures
⏪	⏩
◀	▶
Back	Close
Full Screen / Esc	
Printer-friendly Version	
Interactive Discussion	

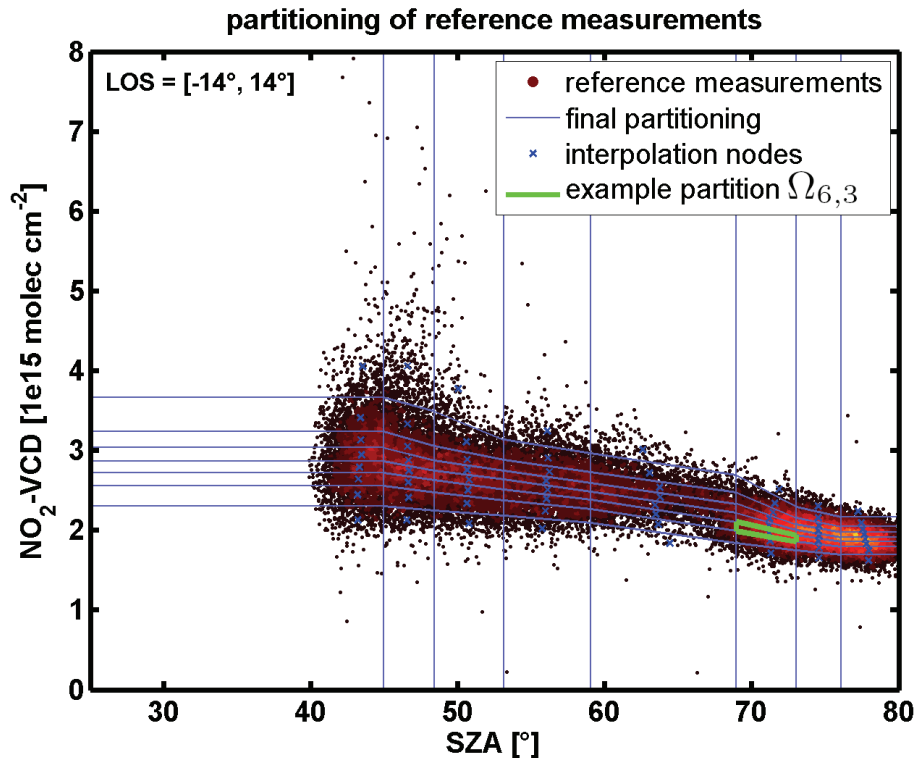


Fig. 4. Partitioning of GOME-2 reference measurements (color-coded density) in the (ϑ, V_N) -plane for the near-nadir direction ($|\psi| \leq 14^\circ$) for 25 March 2009. Each partition contains an almost equal number of measurements from which BrO/O₃ SCD ratios are retrieved. The example partition $\Omega_{6,3}$ is depicted in Fig. 5. The mean of measurements within each partition (blue crosses) are used as nodes for interpolating the results (Fig. 6).

Tropospheric BrO in the Arctic: satellite retrieval and ground-based data

H. Sihler et al.

Title Page

Abstract Introduction

Conclusions References

Tables Figures

◀ ▶

◀ ▶

Back Close

Full Screen / Esc

Printer-friendly Version

Interactive Discussion



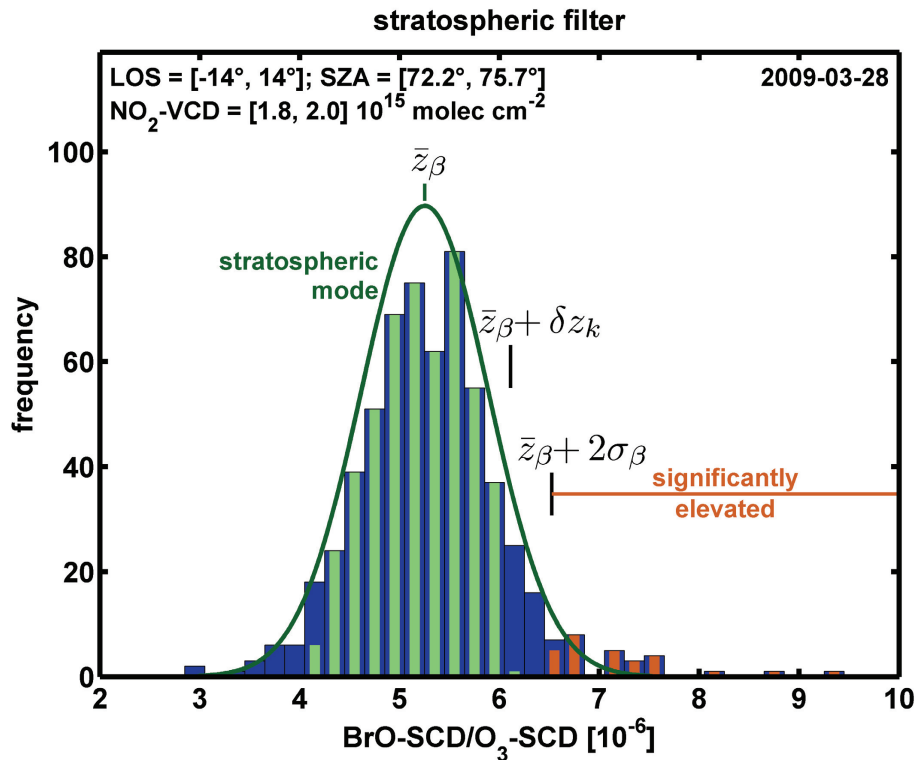


Fig. 5. Frequency distribution of measured BrO-SCD to O₃-SCD ratios (blue) from the example partition $\Omega_{6,3}$ in Fig. 4. The algorithm retrieves the limits of a subdivision with minimal asymmetry (green) containing mostly measurements of the stratospheric background. Significantly enhanced measurements (high BrO, low O₃) appear in the right tail of the distribution (red). See text for details.

Tropospheric BrO in the Arctic: satellite retrieval and ground-based data

H. Sihler et al.

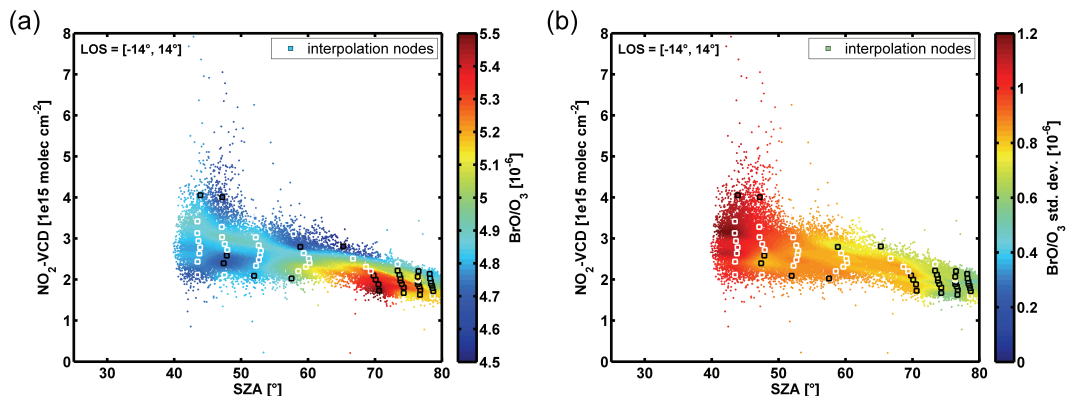


Fig. 6. Interpolation **(a)** of the BrO/O₃ SCD ratio surface and **(b)** its standard deviation σ depending on SZA and NO₂ VCD. The nodes of the bilinear surface interpolation (squares) are the mean of the partitions displayed in Fig. 4. The distributions of some partition with a negligible asymmetry are not filtered before the interpolation and indicated by white squares.

Title Page

Abstract

Introduction

Conclusions

References

Tables

Figures

◀

▶

◀

▶

Back

Close

Full Screen / Esc

Printer-friendly Version

Interactive Discussion

Tropospheric BrO in the Arctic: satellite retrieval and ground-based data

H. Sihler et al.

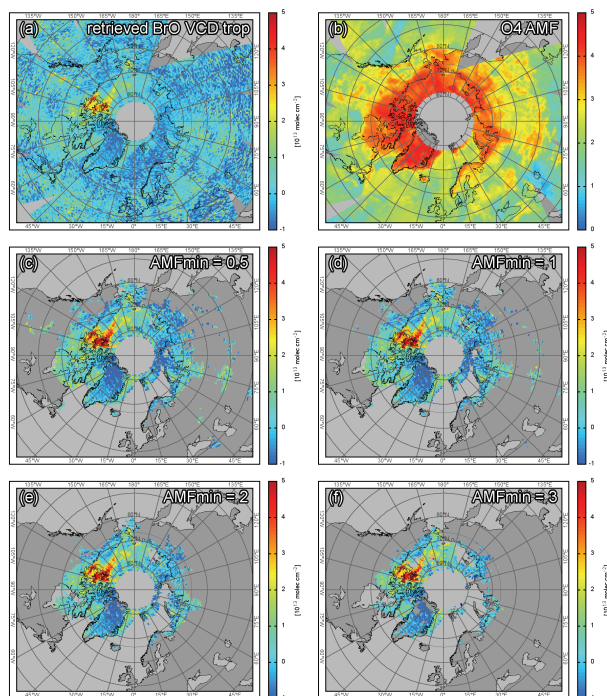


Fig. 7. Illustration of the sensitivity filter and tropospheric AMF applied on GOME-2 measurements for 25 March 2009 (same as Fig. 1). **(a)** The retrieved tropospheric BrO VCDs are filtered according to the respective minimum sensitivity to trace gas concentrations close to the surface using **(b)** measured AMFs of O_4 . Panels **(c)** through **(f)** show tropospheric BrO VCDs for different sensitivity thresholds $AMF_{500}^{\min} = 0.5, 1, 2, 3$, respectively. Note that the sensitivity to the choice of AMF_{500}^{\min} is low. **(a)** is calculated using A_{geom} , **(c)–(f)** are calculated using A_{500} . Areas without any sensitive measurements are left gray.

Title Page

Abstract

Introduction

Conclusions

References

Tables

Figures

◀

▶

◀

▶

Back

Close

Full Screen / Esc

Printer-friendly Version

Interactive Discussion

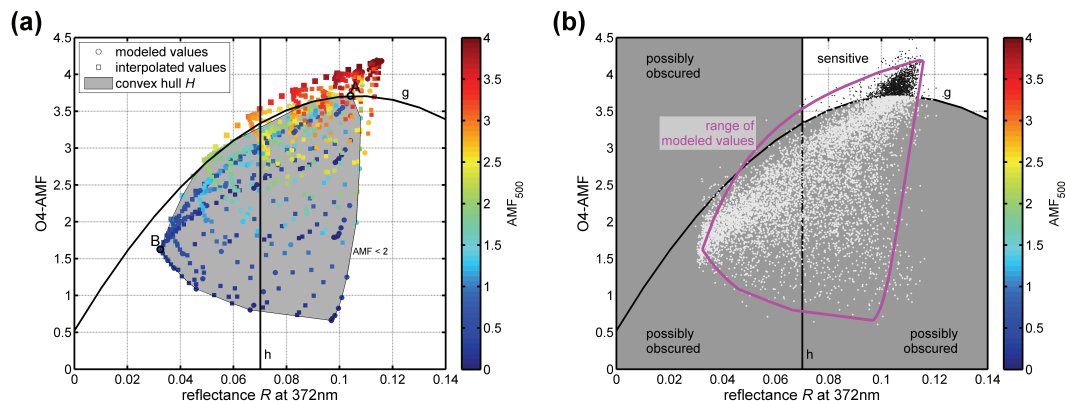


Fig. 8. (a) Modelled and interpolated (R , A_0 , A_{500})-triplets for a nadir geometry at $SAZ = 66^\circ$. The convex hull H (shaded area) including all $AMF_{500} < 2 = AMF_{500}^{\min}$ is parameterised in order to provide a threshold for the surface sensitivity filter. (b) Classification of all GOME-2 nadir observations of 2008 at the same SAZ based on measured R and A_0 with a threshold of $AMF_{500}^{\min} = 2$. The described filter distinguishes between measurements sensitive to the lowest 500 m of the atmosphere (black dots) and those that are possibly obscured by clouds and/or too low albedo (grey area, bright dots). The convex hull (magenta) of modelled values contains approx 94 % of the measurements.

Tropospheric BrO in the Arctic: satellite retrieval and ground-based data

H. Sihler et al.

Title Page

Abstract

Introduction

Conclusions

References

Tables

Figures

◀

▶

◀

▶

Back

Close

Full Screen / Esc

Printer-friendly Version

Interactive Discussion

Tropospheric BrO in the Arctic: satellite retrieval and ground-based data

H. Sihler et al.

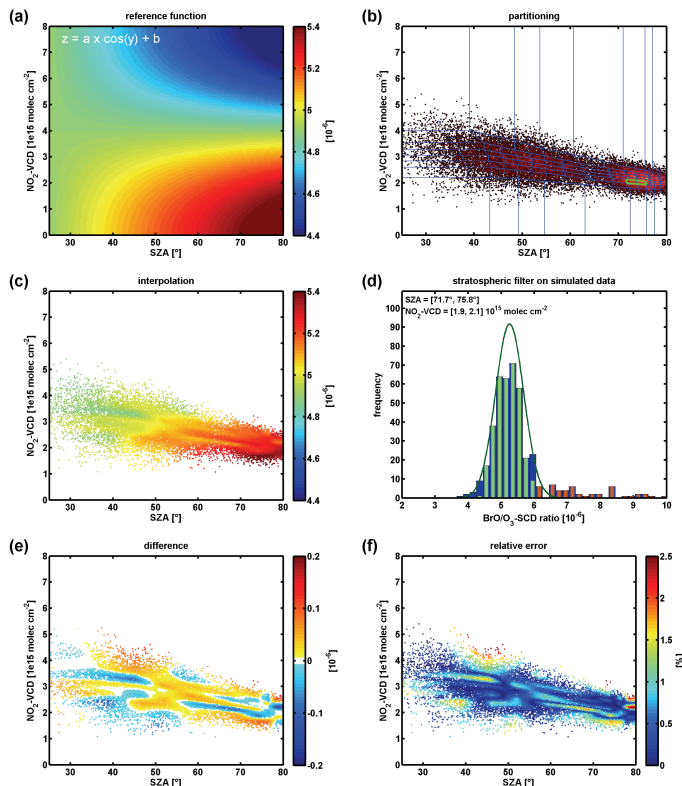


Fig. 9. Benchmark of the separation algorithm (Sect. 2.2 and Appendix A) using simulated measurements modelling a **(a)** known surface. **(b)** Partitioning of measurements, **(c)** interpolated surface nodes, **(d)** application of asymmetry-filter. **(e)** The difference between true and retrieved surface function shows only small deviations. **(f)** The relative error almost never exceeds 2 %.

Title Page

Abstract

Introduction

Conclusions

References

Tables

Figures

◀

▶

◀

▶

Back

Close

Full Screen / Esc

Printer-friendly Version

Interactive Discussion

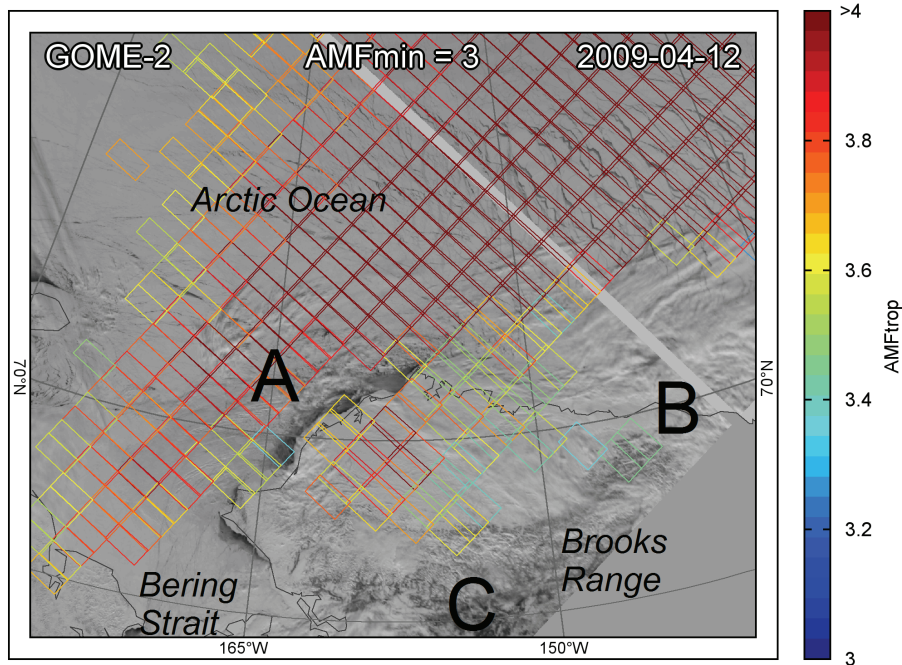


Fig. 10. Overlay image of derived AMF_{500} (color-coded) and AVHRR reflectance measurements (monochrome background, channel 1, 630 nm) over Northern Alaska and the Arctic Ocean. Blue quadrangles indicate GOME-2 satellite pixels with an assured sensitivity to near-surface absorbers ($AMF_{500} \geq 3$). Pixels above leads at the north-west coast of Alaska (**A**), above clouds (**B**), and over the dark Brooks Range (**C**) are labelled possibly obscured ($AMF_{500} < 3$) and not plotted.

Tropospheric BrO in the Arctic: satellite retrieval and ground-based data

H. Sihler et al.

Title Page

Abstract Introduction

Conclusions References

Tables Figures

◀ ▶

◀ ▶

Back Close

Full Screen / Esc

Printer-friendly Version

Interactive Discussion

Tropospheric BrO in the Arctic: satellite retrieval and ground-based data

H. Sihler et al.

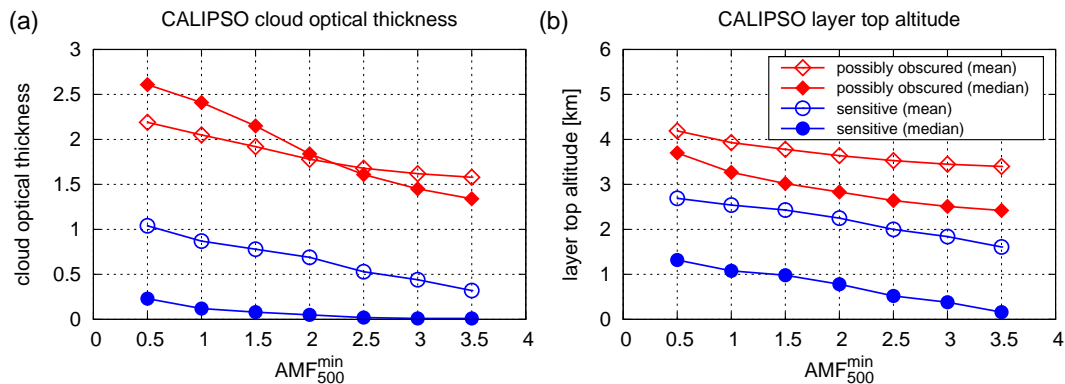


Fig. 11. Mean and median **(a)** cloud optical thickness and **(b)** layer top altitude measured by CALIPSO depending on the sensitivity threshold AMF_{500}^{\min} applied on collocated GOME-2 measurements. Collocated measurement are divided according to the retrieved surface sensitivity: $AMF_{500} > AMF_{500}^{\min}$ (sensitive to the surface; blue circles) and $AMF_{500} < AMF_{500}^{\min}$ (possibly obscured; red diamonds). Note that the difference between mean and median values indicates asymmetric distributions. Error bars are omitted for the sake of clarity.

Tropospheric BrO in the Arctic: satellite retrieval and ground-based data

H. Sihler et al.

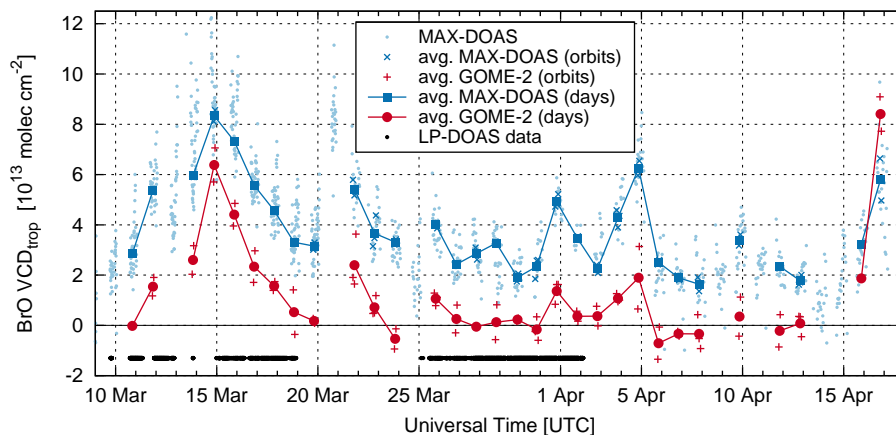


Fig. 12. Time-series of MAX-DOAS BrO VCDs from aboard the Amundsen research icebreaker in 2008 compared to retrieved tropospheric BrO VCDs from GOME-2 ($AMF_{500}^{\min} = 1$), same data as in Fig. 17a. The black dots denote periods of LP-DOAS measurements. Error bars are omitted for the sake of clarity.

[Title Page](#)
[Abstract](#)
[Introduction](#)
[Conclusions](#)
[References](#)
[Tables](#)
[Figures](#)
[◀](#)
[▶](#)
[◀](#)
[▶](#)
[Back](#)
[Close](#)
[Full Screen / Esc](#)
[Printer-friendly Version](#)
[Interactive Discussion](#)

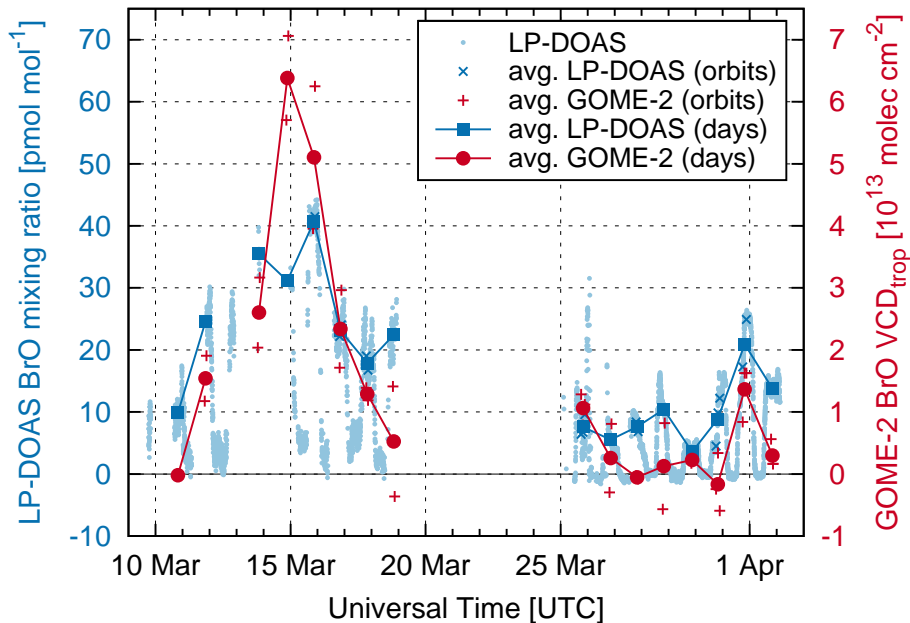


Fig. 13. Same as Fig. 12 but showing BrO mixing ratios measured by LP-DOAS. Both ordinates are scaled corresponding to a mixing height of 345 m. Correlation in Fig. 17b.

Tropospheric BrO in the Arctic: satellite retrieval and ground-based data

H. Sihler et al.

Title Page

Abstract Introduction

Conclusions References

Tables Figures

⏪ ⏩

⏴ ⏵

Back Close

Full Screen / Esc

Printer-friendly Version

Interactive Discussion



Tropospheric BrO in the Arctic: satellite retrieval and ground-based data

H. Sihler et al.

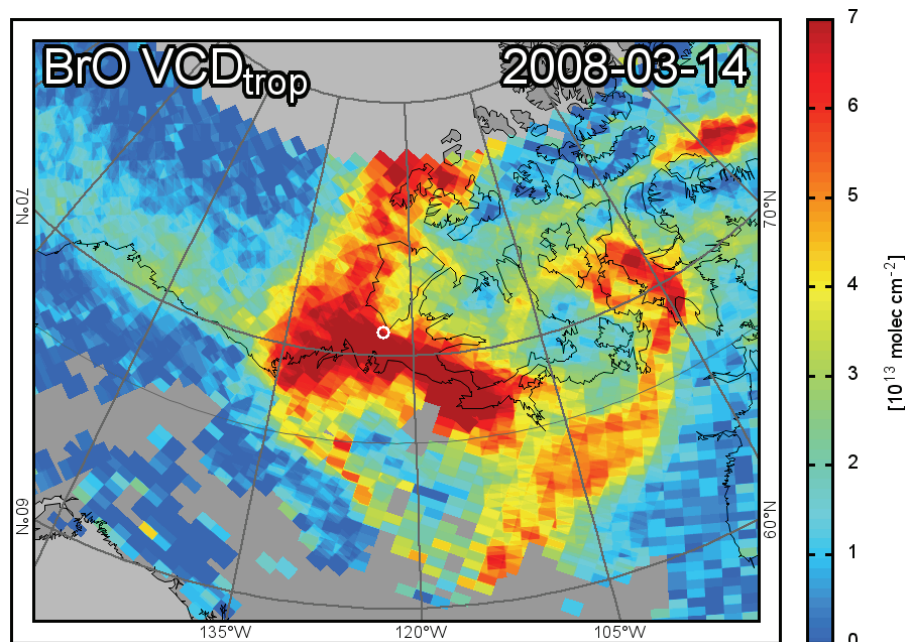


Fig. 14. Satellite map of tropospheric BrO VCDs measured by GOME-2 on 14 March 2008. The circle denotes the position of the Amundsen icebreaker. Further maps of the Amundsen campaign are shown in the Supplement.

[Title Page](#)[Abstract](#)[Introduction](#)[Conclusions](#)[References](#)[Tables](#)[Figures](#)[◀](#)[▶](#)[◀](#)[▶](#)[Back](#)[Close](#)[Full Screen / Esc](#)[Printer-friendly Version](#)[Interactive Discussion](#)

Tropospheric BrO in the Arctic: satellite retrieval and ground-based data

H. Sihler et al.

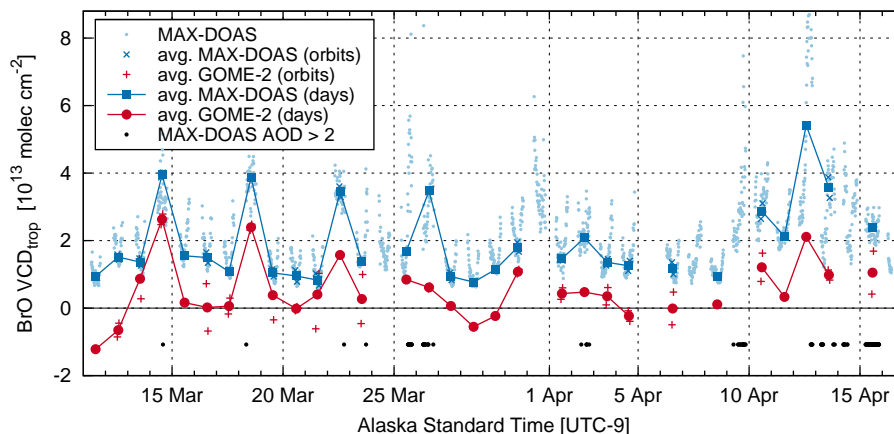


Fig. 15. Time-series of retrieved BrO VCDs from ground-based MAX-DOAS measurements at Barrow, Alaska, 2009 compared to retrieved tropospheric BrO VCDs from GOME-2 ($AMF_{500}^{\min} = 1$), same data as in Fig. 17c. Black dots denote MAX-DOAS measurements, where the surface aerosol optical density (AOD) exceeded 2. Error bars are omitted for the sake of clarity.

Title Page

Abstract

Introduction

Conclusions

References

Tables

Figures

◀

▶

◀

▶

Back

Close

Full Screen / Esc

Printer-friendly Version

Interactive Discussion

Tropospheric BrO in the Arctic: satellite retrieval and ground-based data

H. Sihler et al.

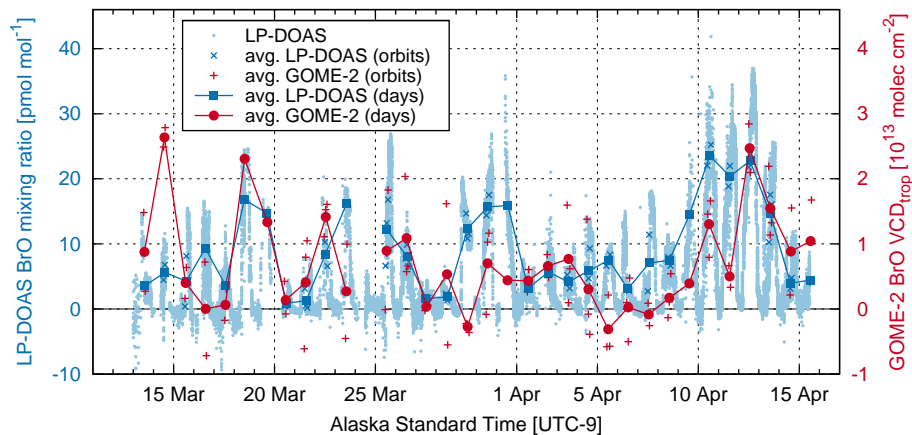


Fig. 16. Same as Fig. 15 but showing BrO mixing ratios measured by LP-DOAS. Both ordinates are scaled corresponding to a mixing height of 345 m. Correlation in Fig. 17d.

Title Page

Abstract

Introduction

Conclusions

References

Tables

Figures

◀

▶

◀

▶

Back

Close

Full Screen / Esc

Printer-friendly Version

Interactive Discussion

Tropospheric BrO in the Arctic: satellite retrieval and ground-based data

H. Sihler et al.

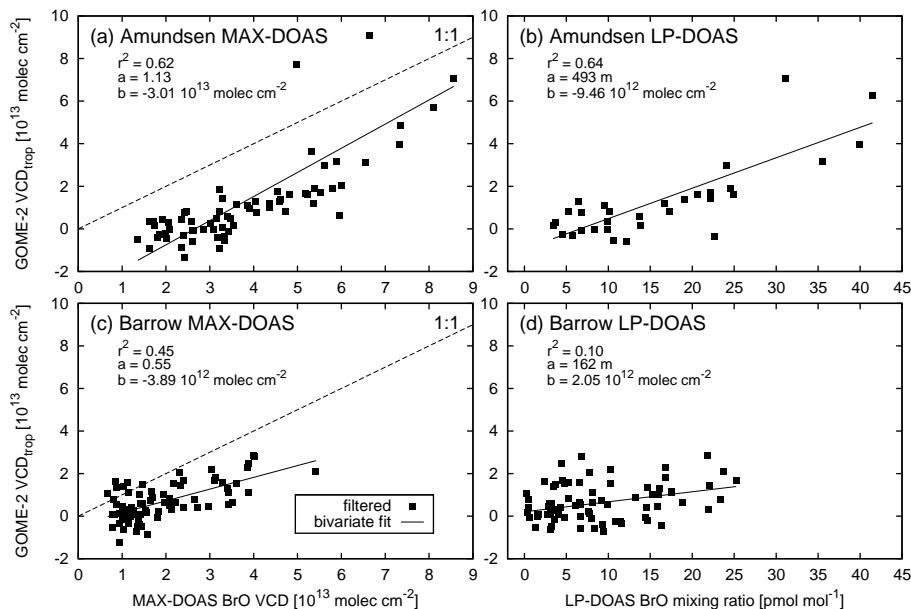


Fig. 17. Correlation and orthogonal fit of the different ground-based data-sets with VCD_{trop} measured by GOME-2 ($\text{AMF}_{500}^{\text{min}} = 1$). Note that the slopes in **(b)** and **(d)** are given in unit metre comparable to the height of the mixing-layer (assuming $\rho_{\text{air}} = 2.9 \times 10^{19} \text{ molec cm}^{-3}$). Error bars are omitted for the sake of clarity.

[Title Page](#)
[Abstract](#)
[Introduction](#)
[Conclusions](#)
[References](#)
[Tables](#)
[Figures](#)
[⏪](#)
[⏩](#)
[◀](#)
[▶](#)
[Back](#)
[Close](#)
[Full Screen / Esc](#)
[Printer-friendly Version](#)
[Interactive Discussion](#)

Tropospheric BrO in the Arctic: satellite retrieval and ground-based data

H. Sihler et al.

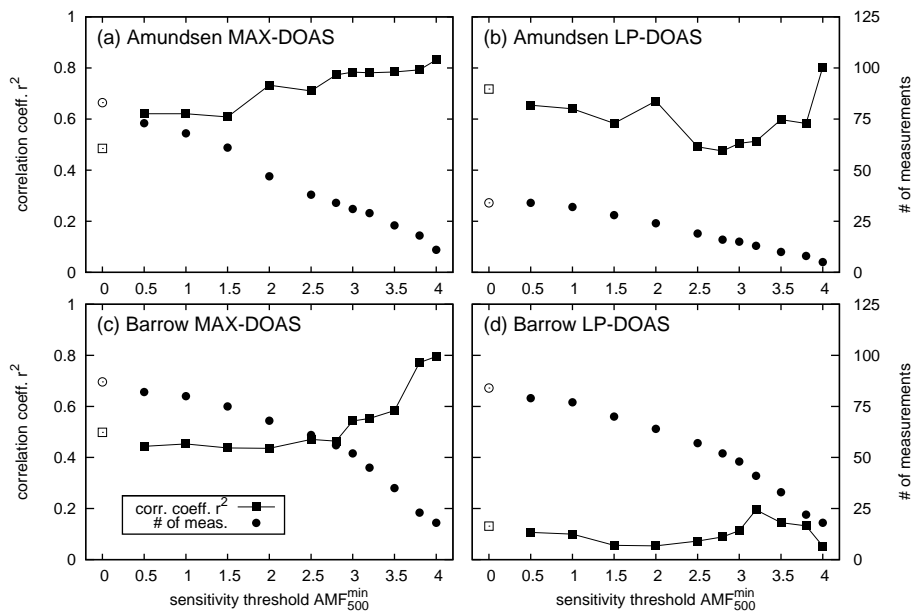


Fig. 18. Correlation coefficient r^2 and number of collocated ground-based and GOME-2 measurements depending on the applied sensitivity threshold AMF_{500}^{\min} . Empty symbols denote correlations without sensitivity filter and geometric AMF applied.

[Title Page](#)
[Abstract](#)
[Introduction](#)
[Conclusions](#)
[References](#)
[Tables](#)
[Figures](#)
[⏪](#)
[⏩](#)
[⏴](#)
[⏵](#)
[Back](#)
[Close](#)
[Full Screen / Esc](#)
[Printer-friendly Version](#)
[Interactive Discussion](#)

Tropospheric BrO in the Arctic: satellite retrieval and ground-based data

H. Sihler et al.

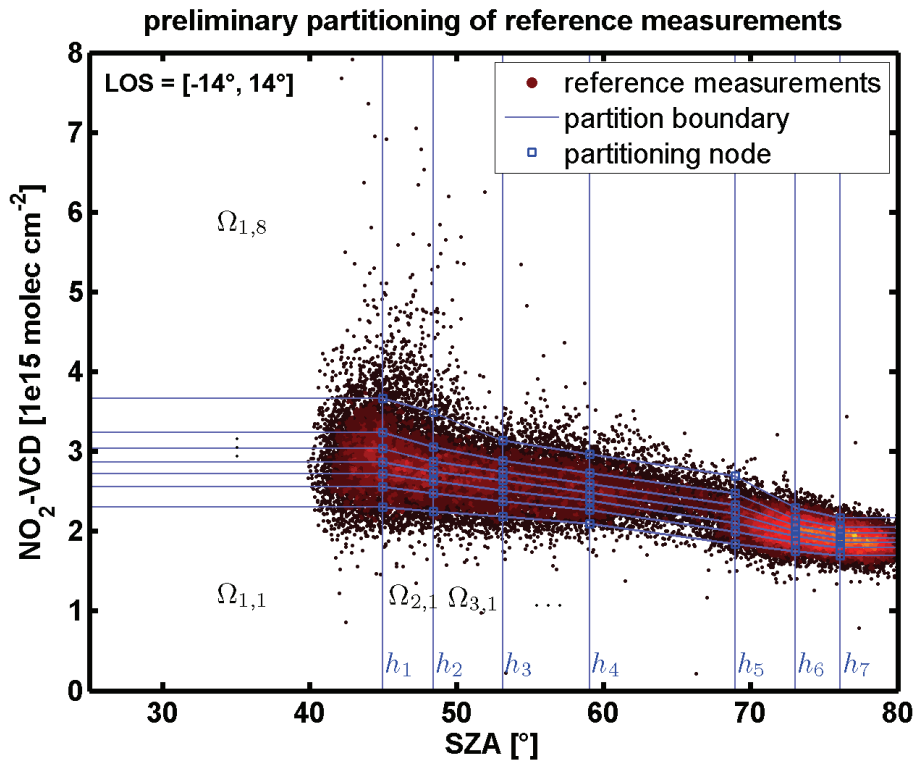


Fig. A1. Preliminary partitioning ($N_{\theta}, N_V = 8$) of GOME-2 reference measurements (color-coded density) for the near-nadir direction ($|\psi| \leq 14^\circ$) whose final partitioning is shown in Fig. 4.

Title Page

Abstract Introduction

Conclusions References

Tables Figures

⏪ ⏩

⏴ ⏵

Back Close

Full Screen / Esc

Printer-friendly Version

Interactive Discussion

